Finanziato dall'Unione europea NextGenerationEU | Ministero dell'Università e della Ricerca | Italiadomani PIANO NAZIONALE DI RIPRESA E RESILIENZA

multi-Risk sciEnce for resilienT commUnities undeR a changiNg climate

Codice progetto MUR: **PE00000005** – CUP LEAD PARTNER: I33C22006910006

Deliverable title: Natural Hazards classification maps of individual network of linear infrastructures – Validation of Methodologies and Application Report

Deliverable ID: DV 6.3.1

Due date: November 2025

Submission date: November 2025

AUTHORS

Pierluigi Claps, Daniele Ganora, Paola Mazzoglio, Giulia Evangelista (POLITO), Francesco Napolitano, Elena Ridolfi, Benedetta Moccia (UNIROMA1), Salvatore Manfreda, Jorge Andres Saavedra Navarro, Angelo Avino (UNINA), Eva Trasforini, Tatiana Ghizzoni, Bruno Colavitto (CIMA), Laura Longoni, Matteo Antelmi, Monica Corti, Lorenzo Panzeri (POLIMI), Paolo De Girolamo, Carolina Codato (UNIROMA1), Lisa Borgatti, Giacomo Titti, Davide Donati (UNIBO), Giorgio Bellotti, Alessandro Romano, Leopoldo Franco, Claudia Cecioni (UNIROMA3), Pasquale Fabio Giuseppe Filianoti (UNIRC), Marcello Di Risio, Davide Pasquali (UNIVAQ).

1. Technical references

Project Acronym	RETURN
Project Title	multi-Risk sciEnce for resilienT commUnities undeR a changiNg climate
Project Coordinator	Domenico Calcaterra UNIVERSITA DEGLI STUDI DI NAPOLI FEDERICO II domcalca@unina.it
Project Duration	December 2022 – November 2025 (36 months)

Deliverable No.	DV6.3.1
Dissemination level*	PU
Work Package	WP3 - Dynamic mapping of natural and climatic hazards over the infrastructure systems
Task	T3.1 - Robust hazard mapping over network infrastructures (link with Spokes 1÷3)
Lead beneficiary	POLITO, UNIROMA1
Contributing beneficiary/ies	POLITO, UNIROMA1, UNINA, CIMA, POLIMI, UNIBO

* PU = Public

PP = Restricted to other programme participants (including the Commission Services)

RE = Restricted to a group specified by the consortium (including the Commission Services)

CO = Confidential, only for members of the consortium (including the Commission Services)

Document history

Version	Date	Lead contributor	Description
0.1	01.11.2025	UNIROMA1 e POLITO	First draft
0.2	12.11.2025	UNIROMA1 e POLITO	Critical review and proofreading
0.3	19.11.2025	POLITO	Edits for approval
1.0	28.11.2025	POLITO	Final version

2. Abstract

Within Task 3.1, dynamic mapping was conducted to reflect the evolving knowledge evolution of the hazard assessment derived from Spokes 1 to 3. The mapping criteria stem from existing robust and reliable methodologies ensuring a reliable classification of hazards affecting key transport and utility infrastructure, including roads, railways, waterways, and the utility grid.
This Task produced methodologies for hazard assessment and natural hazard classification maps for linear infrastructures in the following domains: extreme rainfall (Section 3.1.a), floods (Section 3.1.b), coastal flooding induced by extreme wind waves (Section 3.1.c) and landslides (Section 3.1.d).
This deliverable outlines the products that were developed within Task 3.1 of the Spoke TS2 to achieve these objectives, which can be summarized as follows:

- up-to-date high-resolution national-scale maps of extreme rainfall statistics (Section 3.1.a);
- national-scale inventory of 631 gauged basins with over 100 attributes related to geomorphology, soil, land cover, vegetation, climate, and extreme precipitation (Section 3.1.a);
- methodology for reliably estimating basin flood response time to develop design flood hydrographs in ungauged basins (Section 3.1.a);
- guidelines for evaluating flood-related hazard based on watershed characteristics and on the infrastructure section type (Section 3.1.b);
- national/regional flood scenarios that integrate satellite-derived flood maps and historical flood data in combination with geomorphic basin features and climatic conditions features as inputs for machine learning models (Section 3.1.b);
- a probabilistic risk assessment for isolated areas at regional scale (Section 3.1.b);
- the estimation of coastal flooding areas, induced by extreme waves and water level conditions, with an innovative methodology capable of considering potential MeteOcean scenarios altered by climate changes (Section 3.1.c);
- evaluation of the landslide hazard at a regional scale and its interaction with linear infrastructures, but in current and future scenarios of landslide occurrences (Section 3.1.d).

The methodologies developed in the task are described in the first part of the deliverable (*DV 6.3.1 - Natural Hazards classification maps of individual network of linear infrastructures - Methodology Report*). This second part is instead focused on the implementation process and the key results obtained.

3. Table of contents

List of Figures

List of Tables

3.1 Natural Hazards classification maps of individual network of linear infrastructures

3.1.a Increasing the spatial detail of the hydrological hazard mapping

3.1.a.1 FOCA dataset

3.1.a.1.1 Catchment descriptors

The catchments included in the FOCA dataset (delineated with the methodology described in the first part of the deliverable) cover a wide variety of morphological features and a considerable elevation range (Figure 1a). Figure 1 also shows the empirical cumulative distribution functions (ECDFs) of some key catchment attributes: the area (Figure 1b) and the mean catchment elevation (Figure 1c).

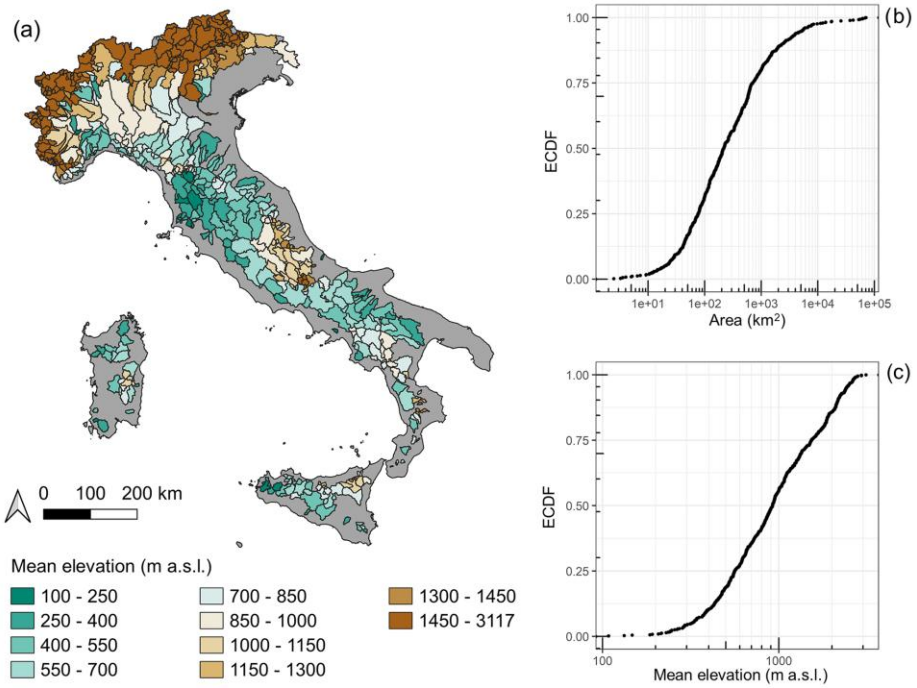

Figure 1. Mean elevation of the 631 catchments (a) and empirical cumulative distribution functions (ECDFs) of some key catchment attributes: area (b) and mean elevation (c). Administrative boundaries: GADM v3.6.

To provide a robust set of catchment features, we have checked the consistency between this new dataset and the previously published one (Claps et al., 2020a, b, c) in terms of catchment areas, which were mostly based on the values published in the hydrologic yearbooks and in *Pubblicazione no. 17*. To set the level of accuracy of the procedures that we used, a 10 % maximum deviation of the difference (positive or negative) was considered acceptable. All the catchments for which the discrepancy is greater than 10 % have been individually re-examined. In some cases, the discrepancy was found to derive from a small shift of the catchment outlets upstream or downstream of a confluence, thus including or excluding relevant sub-catchments.

Another important check has been made: the difference between the length of the main channel (LMC) of each catchment and the length of the longest drainage path (LLDP) was analyzed. Even though these two attributes are well known to have a strong relationship, this connection was not always found in our data: for some catchments, the two lengths were significantly different, even after a thorough manual check. A threshold of a 3 km difference (corresponding to the value that selects the upper 5 % of the catchments with marked differences) was used to identify those catchments for which the difference in length between LMC and LLDP should be further investigated. For those catchments, manual inspections highlighted a drawback in the GIS procedure that produced LMC and LLDP measurements with unrealistic discrepancies. Two

different cases were observed. In one case, the resulting main channel shapefile consisted of a polygonal chain made up of multiple features that needed to be merged into one. In the other case, multiple LLDPs that differed from each other by no more than 100 m (2–3 pixels) were identified for the same catchment. In the latter case, one LLDP was manually chosen and the other ones were removed. We also observed that the two situations could occur simultaneously.

To get a general feel for the consistency of these two attributes, some scaling laws for the drainage network can be employed. One of the best-known is Hack's law (Hack, 1957; Eq. 3). A log-log scatter plot between main channel length and basin area for all 631 catchments is displayed in Figure 2, where panels (a) and (b) refer to the results before and after the quality control, respectively. By means of the abovementioned comparisons, we were able to double-check the consistency between the two attributes; we found errors of up about 20 km, which we checked and corrected.

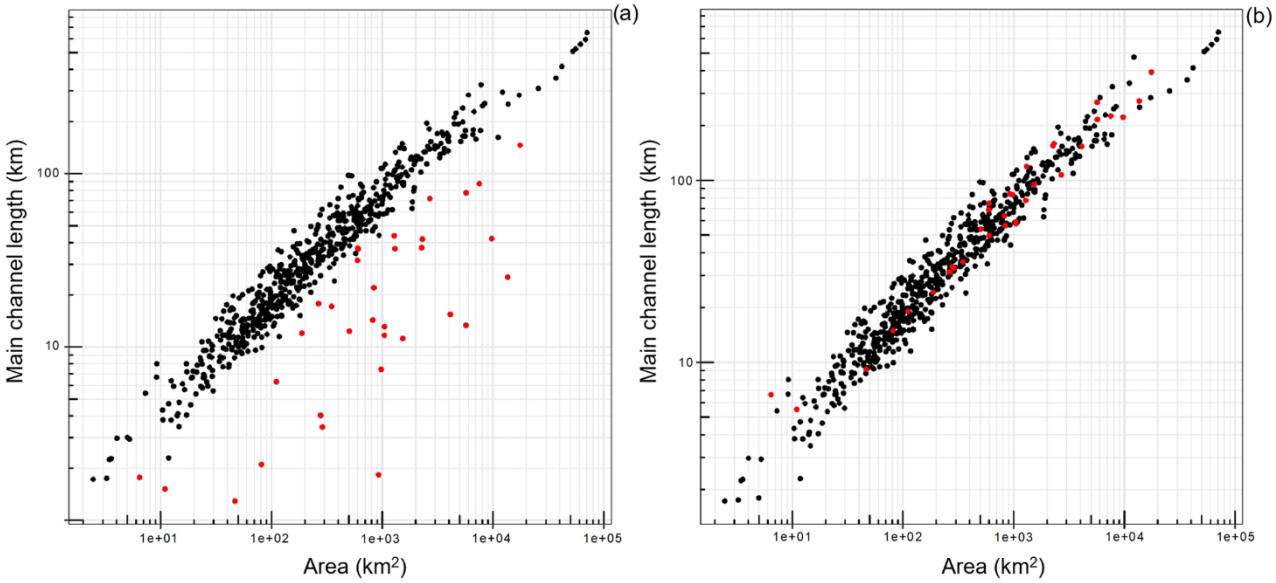

Figure 2. Scaling law between main channel length and basin area for the 631 catchments before (a) and after (b) the quality-control procedure for LLDP and LMC.

For all the attributes, a spatial average value is provided, along with an additional assessment of the spatial variability in terms of the (spatial) coefficient of variation. On the other hand, the temporal variability is not considered here. The only exceptions are the coefficient of variation of the NDVI (normalized difference vegetation index) and the coefficient of variation of the rainfall regimes. The spatial coefficient of variation can thus be considered a proxy for the uncertainty associated with the use of a mean value for the entire catchment. This statistic is additional information that is not usually reported in the CAMELS datasets, but it represents added value here, especially for a nation with such a complex geomorphology and climate as Italy.

3.1.a.1.2 Data availability

The dataset detailed in this work is available at https://doi.org/10.5281/zenodo.10446258 (Claps et al., 2023). It contains all the catchment boundaries and related catchment attributes described before. In case of future updates, to access the latest version of the database, readers can refer to https://doi.org/10.5281/zenodo.8060736 to download the most recent version.

More information on this work is available in Claps et al. (2024).

3.1.a.2 Flood response time in ungauged basins

The robustness of the 29 selected formulas was assessed based on three criteria derived from literature observations (Leopold and Maddock, 1953; Jowett, 1998):

1. Velocity Magnitude: Are the calculated values reasonable?
2. Velocity Behavior: Does velocity increase with basin area, as observed?
3. Velocity Growth Rate: Does the rate of increase match observations?

Velocity magnitude and range

Observed flood flow velocities generally range between 0.5 and 3 m/s. Most formulas yielded estimates within these boundaries. However, formulas by Linsley et al. (1958), Schulz (1969), and Williams (1968) provided velocities up to 6 m/s for larger basins, suggesting they might be unreasonable in magnitude.

Velocity scaling with basin size

Hydraulic geometry studies show that average flow velocity generally increases slightly downstream (i.e., with increasing basin size), as shown in Figure 3. This increase occurs because the rise in flow depth overcompensates for the decrease in river slope. Observations suggest that the velocity growth rate with area should exhibit an exponent of 0.1±0.025.

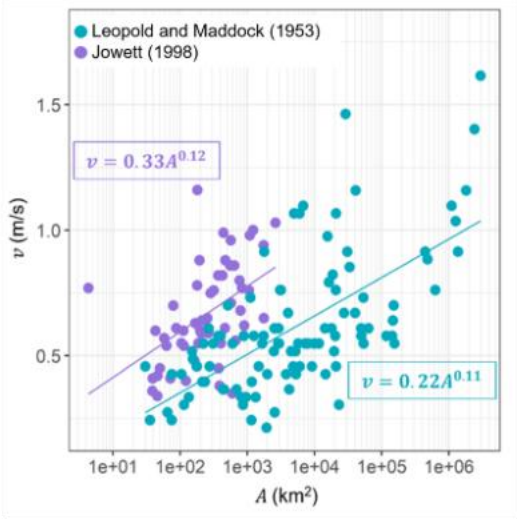

Figure 3. Measured streamflow velocities in river basins in the US (Leopold and Maddock) and in New Zealand (Jowett).

Selection of Robust Formulas

Based on comprehensive assessment encompassing hydraulic consistency, velocity magnitude, and velocity growth rate, the study identified the following formulas as the most robust:

1. Formulas by Chow (1962) and NERC (1975): These two formulas satisfy all three consistency criteria, including hydraulic consistency and a velocity growth rate exponent consistent with observations (0.095 and 0.124, respectively).
2. Formula of SCS (1972): This formula provides velocity estimates that are fully consistent with observations. Its apparent non-compliance with the 2:1 ratio is likely masked by the inclusion of the Curve Number (CN) input, which is correlated with slope.
3. Formulas by McEnroe and Zhao (1999) and Watt and Chow (1985): These formulas are deemed reliable, particularly for small basins. Although they result in an almost constant velocity rather than strictly increasing velocity, this behavior is considered acceptable for safety reasons in smaller catchments where hillslope flow is dominant.

As a further contribution, the study derived analytical relationships that explain velocity behavior in hydraulic formulas based on their exponents and the basin's morphological scaling law, linking characteristic catchment lengths and slopes. The derived analytical conditions offer guidelines for calibrating new formulas to ensure that predicted velocities increase reasonably with catchment area.

A key finding is that formulas derived purely from fundamental hydraulic equations, such as Chezy/Manning, are expected to predict velocities that decrease with basin size. This apparent contradiction arises because, in real catchments, velocity depends primarily on slope, which decreases downstream, a trend that conflicts with the empirical observations of Leopold and Maddock. This underscores that while the 2:1 ratio (hydraulic consistency) is a useful screening tool, it is not sufficient to ensure realistic velocity behavior.

A specific focus is on the Kirpich formula (Kirpich, 1940). Despite its widespread use, it proved unsuitable for application in north-western Italy because the morphological scaling characteristics of the calibration basins differ substantially from those of the study area. This emphasizes that hydraulic formulas should not be applied indiscriminately in regions where basin morphology deviates from the conditions under which the formula was developed.

3.1.b Enhanced methodologies of flood assessment over network legs

3.1.b.1 Guidelines on the evaluation of the flood-related hazard

This section presents the application of the guidelines developed to evaluate the flood-related hazard that may impact linear transport infrastructures (LTIs). The methodological framework adopted is presented in the methodological deliverable, and it is articulated into three main phases:

- Identification of vulnerable infrastructure segments. This step focuses on detecting sections of land transport networks that may be exposed to water-related hazards, using available national or regional hazard maps, hydraulic modelling results, or other reliable data sources.
- Characterization of hazardous events. Through the analysis of key geomorphic and hydrological parameters - such as slope, watershed concentration time, drainage area, and potential water or debris flow sources - this phase estimates the characteristics of the hazardous events affecting the selected infrastructures. The evaluation is supported by topographic and hydrogeological data, typically derived from a Digital Elevation Model (DEM) or other geospatial datasets.
- Damage scenario identification and hazard classification. In this step, the identified parameters are linked to representative damage scenarios, leading to the assignment of a specific hydraulic hazard class to each infrastructure segment. This classification enables prioritization of interventions and supports the development of targeted risk mitigation and monitoring strategies.

The applications presented here follow the logic outlined above. Within the methodological deliverable framework, the assessment of criticality and the subsequent prioritization of interventions were developed through two complementary approaches:

- a simplified procedure, designed for rapid and large-scale evaluation but still effective in identifying key vulnerabilities;
- an extended procedure, which provides a more detailed, parameter-based assessment of hydraulic hazards.

In this document, both approaches are applied to representative infrastructure types. The extended procedure is applied to a tunnel section of a LTI for assessing the hydraulic hazard and to a road bridge for hydraulic hazard assessment related to erosion at the piers. The simplified approach is applied to two road bridges to illustrate its adaptability to different data availability and site conditions.

First the identification of the at-risk infrastructure and the characterization of the hazardous event have been carried out for the two representative cross sections, i.e. the tunnel and the bridge affected by erosion. These analyses provide the basis for understanding the hydraulic context and boundary conditions of the investigated sites and set the foundation for the subsequent phase of hazard classification and assessment, which will be developed in the following sections.

3.1.b.1.1 Guidelines: extended procedure

3.1.b.1.1.1 Hydraulic hazard assessment in LTI tunnel cross sections

The assessment of hydraulic hazard in tunnel cross sections of linear transportation infrastructures (LTI) presented here follows the procedure outlined in the document “Linee Guida per la classificazione e gestione del rischio, la valutazione della sicurezza ed il monitoraggio delle gallerie esistenti” (in Italian) issued by the Italian Ministry of Infrastructure and Sustainable Mobility (Ministero delle Infrastrutture e della Mobilità Sostenibili, 2022). This framework provides a systematic method for classifying the hydraulic hazard of existing tunnels by combining both surface and subsurface water contributions. Although the reference material is issued by the Italian Ministry of Infrastructure and Transport and it has been applied to the Italian peninsula, the methodology can be applied in any context, as it relies on universally known hydrological and hydrogeological parameters.

According to the guidelines, the hydraulic hazard of an LTI tunnel cross section is evaluated through two complementary components: superficial inflows and subsurface inflows. Each component is described by

a set of primary and secondary parameters, which are assigned qualitative classes (low, medium, high) according to reference thresholds provided in the guidelines. The combination of these classes through specific matrices allows for the determination of both partial and overall hazard levels.

For superficial inflows, the two key parameters are:

- Rainfall intensity, typically derived from Intensity-Duration-Frequency (IDF) curves for a design rainfall event (e.g., 1-hour duration, 20-year return period);
- Contributing surface, representing the portion of terrain that drains toward the tunnel portals or approach cuts.

For subsurface inflows, the relevant parameters are:

- Groundwater or piezometric level, expressed relative to the elevation of the tunnel floor or crown levels, respectively;
- Hydraulic conductivity of the surrounding formations, which can be adjusted according to the effectiveness of the waterproofing system.

Each parameter combination is translated into a hazard class by means of dedicated matrices, which can be summarized as follows. The following tables (Table 1 to Table 5) were extracted from Ministero delle Infrastrutture e della Mobilità Sostenibili (2022), and translated here in English.

Table 1. Classes of concern related to rainfall intensity (reference event: duration = 1 hour, return period Tr = 20 years).

HIGH	>60 mm/h
MEDIUM-HIGH	50-60 mm/h
MEDIUM-LOW	40-50 mm/h
LOW	<40 mm/h

Table 2. Classes of concern related to groundwater / piezometric level.

HIGH	Equal to or above the tunnel crown level
MEDIUM-HIGH	Between the crown level and mid-height of the tunnel
MEDIUM-LOW	Between the mid-height and the tunnel invert level
LOW	Equal to or below the tunnel invert level

Table 3. Hazard classes related to surface inflows based on the combination of rainfall intensity and contributing surface area.

Precipitation intensity	Contributing area	Hazard Class
HIGH	HIGH	HIGH
	MEDIUM	
	LOW	
MEDIUM–HIGH	HIGH	
	MEDIUM	MEDIUM–HIGH
	LOW	
MEDIUM–LOW	HIGH	
	MEDIUM	MEDIUM–LOW
	LOW	
LOW	HIGH	
	MEDIUM	LOW
	LOW	

Table 4. Hazard classes related to subsurface inflows based on the combination of groundwater/piezometric level and hydraulic conductivity/waterproofing defect.

Groundwater / Piezometric Level	Hydraulic Conductivity / Waterproofing Defect	Hazard Class
HIGH	HIGH	HIGH
	LOW	MEDIUM-HIGH
MEDIUM–HIGH	HIGH	
	LOW	MEDIUM-LOW
MEDIUM–LOW	HIGH	
	LOW	LOW
LOW	HIGH	
	LOW	

Table 5. Overall hydraulic hazard classes based on the combination of surface and subsurface inflows.

Surface Inflows	Subsurface Inflows	Hazard Class
HIGH	HIGH	HIGH
	MEDIUM-HIGH	
	MEDIUM-LOW	
	LOW	
MEDIUM–HIGH	HIGH	
	MEDIUM-HIGH	MEDIUM-HIGH
	MEDIUM-LOW	
	LOW	
MEDIUM-LOW	HIGH	HIGH
	LOW	MEDIUM-HIGH
	HIGH	MEDIUM-LOW
	MEDIUM-HIGH	
LOW	MEDIUM-LOW	HIGH
	LOW	MEDIUM-HIGH
	HIGH	MEDIUM-LOW
	MEDIUM-HIGH	LOW

The process therefore is defined by three main steps:

- assess the partial hazard from superficial inflows, based on rainfall intensity and contributing surface area;
- assess the partial hazard from subsurface inflows, based on groundwater level and hydraulic conductivity;
- combine the two partial results to obtain the overall hydraulic hazard class for the cross section.

This semi-qualitative approach allows for a consistent and transparent evaluation of hydraulic hazard even in cases where detailed hydrological data are limited, offering a standardized methodology for comparing different tunnels or prioritizing further investigations.

To demonstrate the practical application of the methodology, a generic LTI tunnel cross section located in Italy is considered as a representative case. The example refers to a 600-meter-long single-carriageway tunnel situated in a hilly area of central Italy, characterized by alternating gravelly-sandy deposits and fractured rock, both of which display high hydraulic conductivity. The tunnel is equipped with longitudinal drains and side channels, but no continuous interception trench or upstream cutoff structure is present.

The local hydroclimatic setting is typical of the region, with intense but short-duration rainfall events during autumn and winter and dry conditions in summer. Based on regional IDF curves, the rainfall intensity for a one-hour storm with a 20-year return period is estimated at approximately 55 mm/h. According to Table 1 of the Italian guidelines, this corresponds to a medium-high intensity class.

The contributing surface draining toward the tunnel includes not only the portals and approach cuts but also adjacent road sections, since no protective ditches or diversion systems are in place. Consequently, this

parameter is classified as high. When combined using the matrix for superficial inflows (Table 2), the resulting hazard class for surface water is medium-high.

For subsurface inflows, the groundwater table is assumed to lie at or slightly above the tunnel crown level, corresponding to a high class for groundwater level (Table 3). The surrounding formations have high hydraulic conductivity, and the waterproofing system is only partially effective. Using the subsurface inflow matrix (Table 4), the resulting hazard class for groundwater inflows is high.

The overall hydraulic hazard is then determined by combining the two partial assessments - superficial inflows (medium-high) and subsurface inflows (high) - using the final classification matrix (Table 5). The resulting overall hydraulic hazard class is high.

This outcome represents a realistic scenario for Italian tunnels, particularly those located in permeable formations and exposed to intense rainfall. The combination of a large contributing surface, high-intensity precipitation, shallow groundwater, and limited waterproofing capacity leads to elevated vulnerability to both surface and groundwater inflows.

3.1.b.1.1.2 Hydraulic hazard assessment for scour at bridge piers

The assessment of hydraulic hazard related to scour phenomena at bridge piers follows the methodology described in the "Istruzioni Operative per l'applicazione delle Linee Guida per la classificazione e gestione del rischio, la valutazione della sicurezza ed il monitoraggio dei ponti esistenti" (ANSFISA - Agenzia Nazionale per la Sicurezza delle Ferrovie e delle Infrastrutture Stradali e Autostradali, 2022).

The guidelines are provided in Italian, however they can be applied to any bridge section. According to these Operational Instructions, two main types of erosion processes must be evaluated in bridge hydraulic vulnerability assessments: generalized erosion and localized erosion.

Generalized erosion refers to the lowering of the riverbed in the bridge reach, resulting from the overall contraction of the hydraulic cross-section due to the bridge structure. Localized erosion, instead, develops around piers and abutments because of local turbulence and vortices generated by the interaction between flow and structural elements. Both phenomena can compromise the stability of the foundations and must be analyzed separately, then combined in a comprehensive hazard evaluation.

For generalized erosion, the ANSFISA Operational Instructions (Section 4.5.1.6–4.5.1.7) define two geometric contraction factors that describe the narrowing of the active river section and the floodplain. These are expressed as:

$$C_a = \frac{W_{a,l}}{W_a} \times 100 \quad (3.1.1)$$

$$C_g = \frac{W_{g,l}}{W_g} \times 100 \quad (3.1.2)$$

where:

- C_a: contraction factor of the incised channel;
- C_g: contraction factor of the floodplain area;
- $W_{a,l}$: width of the incised channel occupied by piers and abutments;
- W_a: total width of the incised channel upstream of the bridge;
- $W_{g,l}$: width of the floodplain occupied by embankments, abutments, or approach fills;
- W_g: total floodplain width upstream of the bridge (sum of left and right floodplains).

The geometric quantities are defined depending on the type of river cross-section, as illustrated in Figure 4, Figure 5 and Figure 6.

Rivers with floodplains

The floodplain width W_g is obtained as the sum of left and right floodplains ($W_{g,l} + W_{g,2}$). The incised channel width W_a is measured between the riverbanks. $W_{a,l}$ and $W_{g,l}$ are determined as the widths obstructed by structural components and embankments.

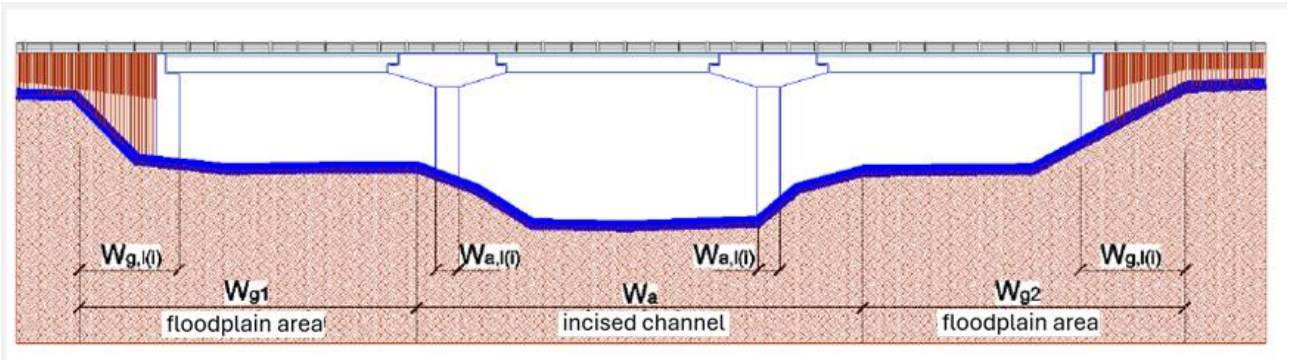

Figure 4. Rivers with floodplains.

Rivers without floodplains

Only the main channel width W_{aand} its obstructed portion $W_{a,l}$ are defined. In this case, C_g cannot be calculated, and for hazard classification, the last column of Table 4.22 of the ANSFISA Operational Instructions (corresponding to C_g <15%) is used.

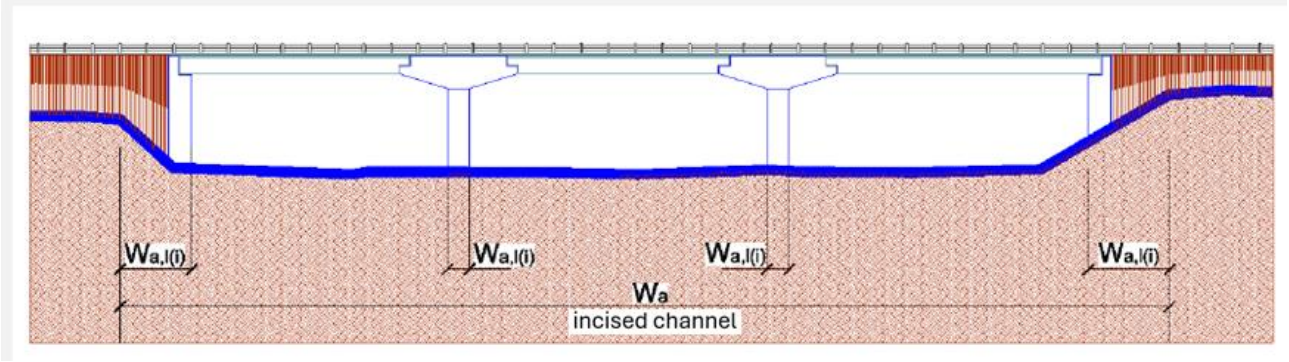

Figure 5. Rivers without floodplains.

Entrenched rivers between valley slopes

The channel is confined between steep banks, without floodplains. The width W_a corresponds to the total active flow width for the design flood stage.

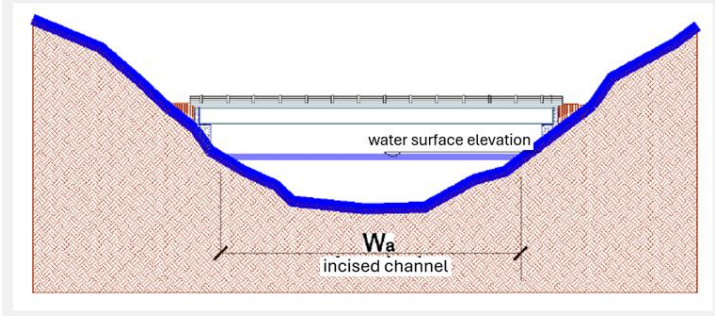

Figure 6. Entrenched rivers between valley slopes.

Once C_a and C_g are determined, the hazard class for generalized erosion is identified using Table 6, which assigns the hazard level based on the combination of the two contraction factors.

Table 6. Hazard class related to the generalized erosion phenomenon.

C_a	C_g				
	>45%	35–45%	25–35%	15–25%	<15%
>35%	HIGH				
25–35%	HIGH		MEDIUM–HIGH		
15–25%	HIGH		MEDIUM–HIGH	MEDIUM	
10–15%	HIGH	MEDIUM–HIGH	MEDIUM	MEDIUM–LOW	
<10%	HIGH	MEDIUM–HIGH	MEDIUM	MEDIUM–LOW	LOW

For localized erosion, the Local Erosion Index (IEL) is defined as:

$$IEL = \frac{d_s}{d_f} \tag{3.1.3}$$

where d_s is the maximum scour depth at the pier or abutment and d_f is the foundation embedment depth below the riverbed. When site-specific or design data are unavailable, the Operational Instructions (Sections 4.5.1.8–4.5.1.9) recommend adopting empirical approximations:

- for circular piers, $d_s = 2a$, where a is the pier radius.
- for abutments, d_s is approximately twice the characteristic width of the abutment.
- for foundations, d_f is the vertical distance between the riverbed and foundation base, or half of the pile length (minimum 4 m if unknown).

The IEL value is compared with Table 7, which defines the hazard levels as follows.

Table 7. Hazard class for the localized erosion phenomenon.

HIGH	$IEL > 1.2$
MEDIUM-HIGH	$1.00 < IEL \leq 1.2$
MEDIUM	$0.80 < IEL \leq 1.00$
MEDIUM-LOW	$0.80 < IEL \leq 0.60$
LOW	$IEL < 0.60$

3.1.b.1.1.3 Extended procedure: Test case 1

The test bridge section belongs to a critical linear transport infrastructure (LTI) and it was built to cross a river incised between valley slopes, typical of Italian mountainous and hilly contexts. The absence of floodplain areas indicates that only the main channel contraction factor C_a is relevant.

For the considered bridge, consisting of three 20 m spans and two circular piers (diameter 2.0 m) located in the main channel, the geometry is as follows:

- total incised channel width: W_a = 40" m";
- width occupied by piers and abutments: $W_{a,l}$ = 12" m".

Hence, the contraction factor is:

$C_a = 12/40 \times 100 = 30\%$

Since no floodplains are present, C_g is undefined and, following the ANSFISA criteria, the hazard classification refers to the last column of Table 6 (for $C_g < 15\%$), resulting in a medium-high hazard class for generalized erosion.

The localized erosion was evaluated using the computed scour depth at the piers. For a 50-year return period, the maximum scour depth is d_s = 2.17" m", and the foundation embedment is d_f = 3.0" m", giving:

IEL = 2.17/3.0 = 0.72

This corresponds to a Medium-low hazard class (Table 7). For a 20-year return period, the scour depth slightly decreases to d_s = 2.21" m", yielding IEL = 0.74, which remains in the same class.

Therefore, for this entrenched river cross-section:

- generalized erosion hazard: Medium-high;
- localized erosion hazard: Medium-low.

This configuration highlights that in confined channels without floodplains, flow acceleration increases contraction effects during floods, while adequate foundation depth provides sufficient safety margin against local scour. The long-term monitoring of bed degradation and foundation exposure is thus recommended.

3.1.b.1.1.4 Extended procedure: Test case 2

To illustrate the application of the methodological framework for the assessment of erosion at bridge foundations, the following section presents a case study concerning a bridge crossing located along a river reach potentially affected by scour phenomena.

The selected case represents an hydraulic condition, corresponding to a flood event with a return period of 50 years (Tr = 50 years) and a discharge of 500 m³/s. This scenario was used to demonstrate the interpretation of the main hydraulic and morphological parameters that control the development of scour around bridge piers and abutments.

The methodology was applied to a representative bridge cross-section, characterized by sharp-nose piers and a coarse-grained riverbed, whose geometry makes it particularly prone to both generalized and localized erosion phenomena.

For this case, the analysis considered the combined effects of flow contraction and local acceleration around the structural elements, using the parameters and equations introduced in the methodological deliverable. The results obtained for the different components of the erosion process are summarized in Table 8.

Table 8. Excavation values for Tr = 50 years.

Parameter	Description	Value (m)
Ys	Mean general scour depth	0.57
Y piers	Scour depth at piers	2.17
Abut left	Scour depth at left abutment	3.34
Abut right	Scour depth at right abutment	5.47
Combined	Representative total scour depth	2.17

The results show that the generalized erosion (Ys = 0.57 m) produces a moderate lowering of the riverbed due to flow contraction, while the localized erosion at piers (2.17 m) represents the main component of scour in the central part of the structure. The maximum excavation depth (5.47 m) occurs near the right abutment, where the flow concentration and secondary circulation patterns enhance sediment removal. The left abutment shows a smaller, though still relevant, scour depth of 3.34 m, consistent with asymmetric flow distribution within the section.

The combined scour depth (2.17 m) can be considered a representative value for the overall erosion effects in this hydraulic condition.

In terms of hydraulic vulnerability, the results suggest a moderate level of hazard, with medium-high predisposition to erosion (PPE) due to the combination of generalized and local scour, medium terrain stability (TR) linked to partial confinement of the flow, and high foundation quality (FQ), since the structural base remains below the maximum scour depth. This translates into a medium RN vulnerability index, consistent with a moderate hydraulic hazard class.

3.1.b.1.2 Simplified procedure

In accordance with the EU Floods Directive 2007/60/EC, River Basin Authorities delineate flood-prone areas under three scenarios: H1 (rare, Tr ≤ 500 years), H2 (frequent, Tr = 100–200 years), and H3 (very frequent, Tr = 20–50 years). These hazard maps, integrated into Flood Risk Management Plans (FRMPs) and updated every six years, provide the reference for identifying land transport infrastructure segments (RSs) exposed to flooding (Samela et al., 2023).

Each RS may fall under multiple hazard levels, as H3 areas are subsets of H2 and H1 zones. Since hydraulic parameters vary across scenarios, flood hazard assessments are performed separately for H1, H2, and H3 to ensure a complete evaluation of flood risks for roads, railways, and other infrastructures.

For each infrastructure section within a flood hazard zone, reference points are defined for geomorphological and hydrological analysis. If the infrastructure intersects the river network, the intersection point serves as the reference. If not, the nearest river point along the steepest downslope path from the segment's downstream end is used.

This ensures spatial consistency in hazard characterization across different infrastructure types.

Debris flow hazards are assessed by identifying potential source areas near infrastructure. These flows typically initiate under intense rainfall in steep, sediment-rich zones. Mapping relies on morphometric parameters (slope, contributing area) derived from DEMs and geological data.

Empirical thresholds suggest initiation occurs for slopes > 27% and contributing areas > 10 ha, with an upper limit of 78% where initiation becomes unlikely (Cavalli et al., 2017; Fannin & Wise, 2021).

To account for runout uncertainty, only sources within 1 km upslope of the infrastructure are considered hazardous (Blais-Stevens & Behnia, 2016; Samela et al., 2023).

Each infrastructure section is analyzed for potential damage mechanisms—including overtopping, infiltration, washout, and debris impact—and assigned a corresponding flood hazard class based on exposure and local hydraulic conditions.

3.1.b.1.2.1 Simplified procedure: test cases

In the following two test cases are presented. The information related to each LTI section is provided in the form of a table and the resulting flood hazard class is reported.

Test case 1 is bridge part of a LTI, the river slope underneath is 3%, the concentration time of the corresponding hydrological basin is 2 hours, the contributing area is 11 hectares, the slope angle is 28%, therefore, according to the guideline, the bridge is classified under flood hazard class III, Table 9.

Table 9. Test case 1: assessment of the flood hazard class given the characteristics of the watershed.

Section type (ex. trench, bridge, tunnel, embankment)		bridge	
River reach number	**River name**	**Section intersecting floodable area**	
1	River 1	River slope (%)	3
		Sub-basin concentration time (h)	2
		Contributing area (ha)	11
		Slopes angle (%)	28
		Flood hazard class	III

Test case 2 is bridge part of a LTI, the river slope underneath is 5%, the concentration time of the corresponding hydrological basin is 2 hours, however, given the elevated slope, the concentration time is irrelevant. The contributing area is 11 hectares, the slope angle is 28%, therefore, according to the guideline, the bridge is classified under flood hazard class I, Table 10. It is worth noting that the only difference between the two bridges river cross sections is the river slope. However, this is sufficient to increase the hazard class.

Table 10. Test case 2: assessment of the flood hazard class given the characteristics of the watershed.

Section type (ex. trench, bridge, tunnel, embankment)		bridge	
River reach number	**River name**	**Section intersecting floodable area**	
2	River 1	River slope (%)	5
		Sub-basin concentration time (h)	2
		Contributing area (ha)	11
		Slopes angle (%)	28
		Flood hazard class	I

3.1.b.1.3 Value and applicability

The proposed guidelines are designed to evaluate flood-related hazards that may affect linear transport infrastructures (LTIs). They were tested on sections of both a railway and a highway in the Calabria Region (southern Italy) to assess their reliability and robustness. The main advantage of the approach lies in its simplicity and adaptability: it can be easily applied to a wide range of case studies. The use of commonly available and widely accessible data and variables ensures the procedure's broad applicability.

These guidelines provide practical support for classifying hazard levels and developing consistent assessment methodologies and adaptation strategies. The approach enhances flood risk assessment and long-term infrastructure planning, promoting more resilient and climate-adaptive transport networks. Furthermore, the analysis can assist in identifying suitable locations for new infrastructure by determining alignment segments associated with lower flood hazard levels.

3.1.b.1.4 Limitations

Despite its broad applicability, the procedure is subject to certain limitations related to data availability and quality. The analysis relies on spatial, hydrological, and infrastructural information that may not always be accessible, up-to-date, or consistent across different regions. In areas where detailed flood maps, topographic data, or infrastructure characteristics are lacking, the reliability of the hazard classification may be reduced. Consequently, the absence or uncertainty of key input data can hinder the full implementation of the methodology and affect the accuracy of the results. Addressing these limitations requires improved data collection, harmonization, and sharing among relevant authorities and stakeholders.

3.1.b.2 Flood scenario generation at the national scale under current climate conditions

3.1.b.2.1 Introduction

A flood susceptibility map of the Italian territory is produced by implementing an RF model combined with a multisource flood inventory and geomorphic features spanning hydrologic, topographic, and categorical information. The risk component is expressed in terms of damage using the depth-damage curve developed by the Joint Research Center (European Commission - Joint Research Centre, 2016), where flood water depth is estimated using the GFI approach developed by Manfreda & Samela (2019).

To provide context for this multisource flood inventory, it is essential to understand the nature and historical scope of hydrogeological events in Italy. The inventory built here encompasses river inundations and flash floods (Figure 7). It is primarily based on two spatial datasets: the AVI Database, containing 5,656 unique historical point events predominantly from the 20th century, and the National Flood Database, Italy, which provides polygon data for 330 precisely dated events measuring physical inundated areas up to December 2025. Analysis of this combined inventory reveals a strong seasonal risk peak in autumn, specifically October and November, aligning with historical catastrophes such as the 1966 Florence flood and the 1994 Piedmont flood. Geographically, regions like Piedmont, Lombardy, and Veneto consistently show the highest vulnerability in both historical frequency and recent inundated areas. Acknowledging the limitations of this inventory, such as the potential overestimation of recent event areas due to modern satellite resolution compared to historical ground surveys, is crucial for interpreting the susceptibility models that rely on it.

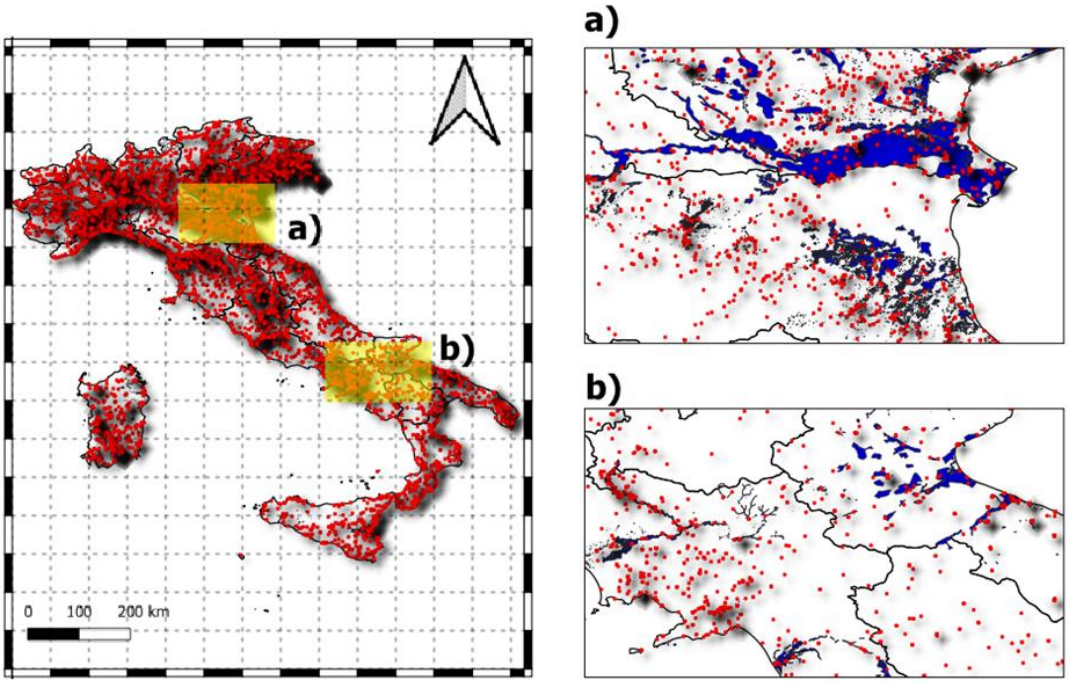

Figure 7. National Flood Database.

The framework considers three main steps, as shown in Figure 8. The first step was the estimation of the flood susceptibility level to derive the flood extension. For this, we work based on the result of Navarro et al. (2025), in which the authors found that a set of nine features outperformed 11 other sets. This set considered the following features: GFI, Elevation, Distance from the Nearest River (DNR), Maximum Mean Daily Precipitation (MMDP), Lithology, Organic matter, Land Cover (LC), NDVI, and Silt.

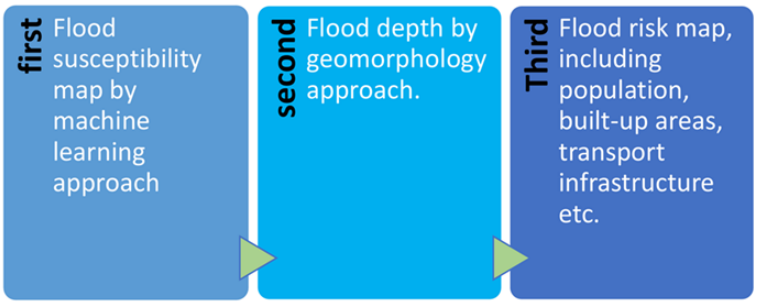

Figure 8. Main components of the flood risk estimation procedure based on the geomorphic approach.

The second step involved the flood water depth estimation by Manfreda & Samela et al. (2019). The process consists of estimating the parameter *a* of the original estimation of GFI (see Samela et al., 2017) calibrating the index. To carry out this, the results from the susceptibility modelling were used. A small area was chosen to show the applicability of this part of the framework.

$$GFI = ln(aA_{river}{}^{n}/HAND) \quad (3.1.4)$$

where A_{river} corresponds to the flow accumulation value in the nearest river, n is equal to 0.354, estimated as the average among values extracted from literature. HAND is defined as the difference in elevation (Nobre et al., 2016) between any location of the basin and the nearest element of the river network identified following the flow path.

Finally, the risk component is expressed in terms of damage using the depth-damage curve developed by the Joint Research Center (European Commission - Joint Research Centre, 2016), where flood water depth is estimated using the GFI approach developed by Manfreda & Samela (2019). These metrics were derived by correlating floodwater depth with exposure classifications based on the characteristics of affected assets, including building category and function (e.g., residential, commercial, industrial) and agricultural land use (crops). Building data was sourced from the DBSN (DataBase di Sintesi Nazionale), while agricultural data was extracted from Corine Land Cover 2018. It is noted that a validation of the damage analysis was not conducted as part of this study due to the scarcity of historical records in Italy.

3.1.b.2.2 Random Forest model and Input Data

Random Forest (RF) is a non-parametric statistical model that employs multiple decision trees combined with the bootstrap aggregating (bagging) approach (Breiman, 1996). This method randomly selects a subset of variables, reducing overfitting effects and improving generalisation. RF offers high performance with few parameters to optimise, also enabling the estimation of variable importance and the use of algorithms for missing value imputation. Breiman (2001) highlights several advantages of RF:

- High efficiency in large datasets
- Ability to handle a high number of variables without losing efficiency
- Estimation of variable importance using different methods
- Generation of an internal estimate of generalisation error (OOB error)
- Relative robustness to outliers and noise
- Low computational cost

The RF model was trained with nine features, each of which is described as follows:

- The Geomorphic Flood Index is a topographic indicator derived from digital elevation models, designed to quantify geomorphic conditions that suggest high flood susceptibility. GFI provides a fast and reliable way to identify flood-prone areas, especially in data-scarce regions, by comparing the relative elevation and position to nearby river channels.

- Elevation is the height above mean sea level and is a fundamental topographic attribute in flood modelling. Lower elevation areas are typically more susceptible to flooding due to proximity to natural water conveyance pathways and floodplains.
- Distance from the Nearest River (DNR) measures the flow path distance from any location to the closest river or stream. Locations closer to rivers are at greater risk for floods, since overflow and flooding usually start from channels and propagate outward, particularly during intense precipitation events.
- Maximum Mean Daily Precipitation (MMDP) refers to the highest average daily rainfall values measured over a given period. It is a critical hydrometeorological factor, as areas experiencing heavier precipitation are more likely to see surface water accumulation and subsequent flooding.
- Lithology represents the physical and chemical composition of surface soils and rocks in a given location. Different lithological units respond variously to infiltration, water retention, and runoff. Coarse gravels may encourage infiltration while clays enhance runoff, amplifying flood risk.
- Organic Matter and Silt. Soil organic matter affects water retention, infiltration, and permeability. Soils rich in organic matter generally have higher permeability and porosity, which can reduce surface runoff and potentially lower local flood risk. Silt is a soil texture class between sand and clay. Soils with high silt content have moderate infiltration and water-holding capacities, which influence the speed and volume of surface runoff following precipitation events. High silt concentrations can therefore affect a region's susceptibility to flooding, depending on its interaction with land cover and precipitation.
- Land Cover (LC) describes the physical material on the land surface, such as vegetation, urban infrastructure, bare soil, or water. Urbanisation increases impervious surfaces, reducing infiltration, increasing runoff, and raising flood susceptibility, while vegetative cover typically mitigates flood risk by improving infiltration and reducing runoff.
- Normalised Difference Vegetation Index (NDVI) is a remote sensing-derived indicator of vegetation health and density. Higher NDVI values correspond to dense, healthy vegetation, which tends to enhance infiltration and decrease surface runoff, resulting in lower flood risk; conversely, low NDVI indicates sparse vegetation and a higher likelihood of flooding.

Each of these features is supported empirically as a key flood conditioning factor in modern machine-learning-based flood susceptibility assessments, providing both environmental and anthropogenic context for robust predictive modelling.

3.1.b.2.3 Depth-Damage Curve and Applicative Example

Depth-damage curves for both residential buildings and agricultural crops were extracted from the Global flood depth-damage functions report (European Commission - Joint Research, 2016). Due to a lack of specific flood damage data in Italy, European-level curves were adopted for both. The analysis applied a power law function for the building curve and an exponential law for the agricultural curve (Figure 9). For the applicative example, a zoomed area was chosen in the Bradano catchment.

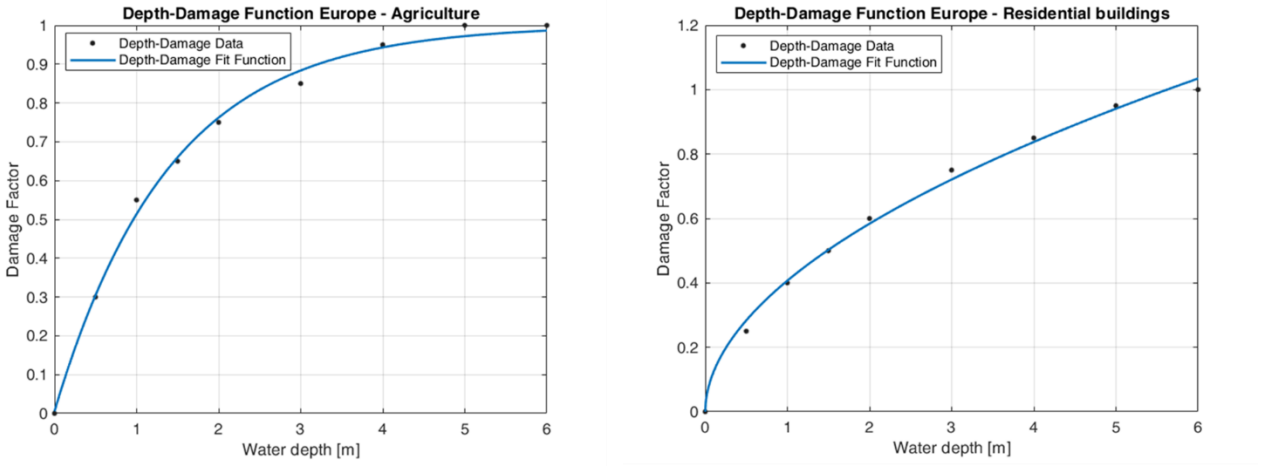

Figure 9. Depth-Damage curves from European Commission - Joint Research (2016) for residential buildings and for agricultural crops.

3.1.b.2.4 Results and Concluding Remarks

The results for the RF model in the evaluation metrics (AUC, Specificity, Sensitivity, and Kappa) provide crucial information. The model achieves a high performance with a value of AUC of 0.95, specificity of 0.87, sensitivity of 0.88 and a kappa index of 0.76. The resulting susceptibility map (Figure 10) is classified into five categories—very low, low, medium, high, and very high—using the quantile method. Figure 11 provides a further breakdown of these susceptibility levels as percentages within each district.

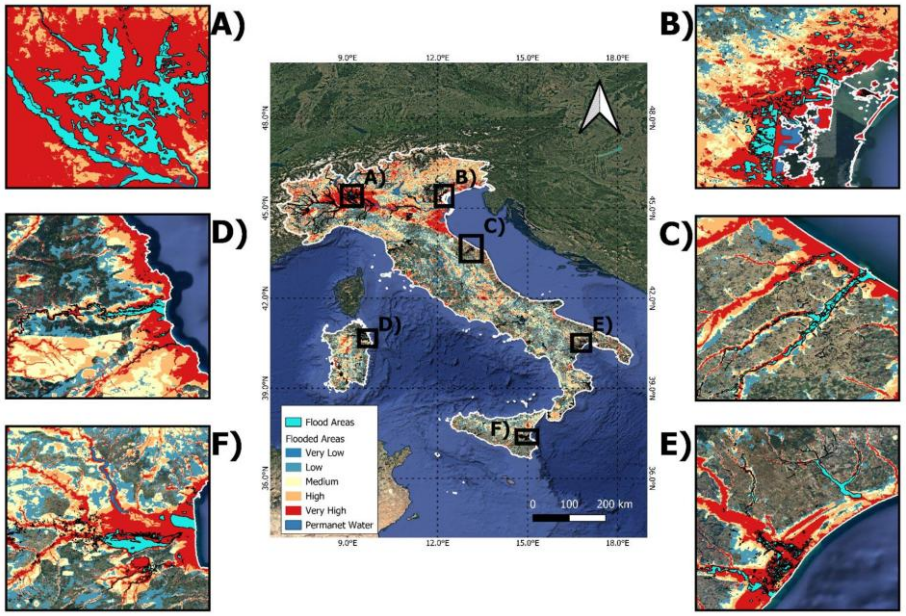

Figure 10. Flood Susceptibility Map of the entire Italian territory, featuring six insets that provide detailed views (Navarro et al., 2025).

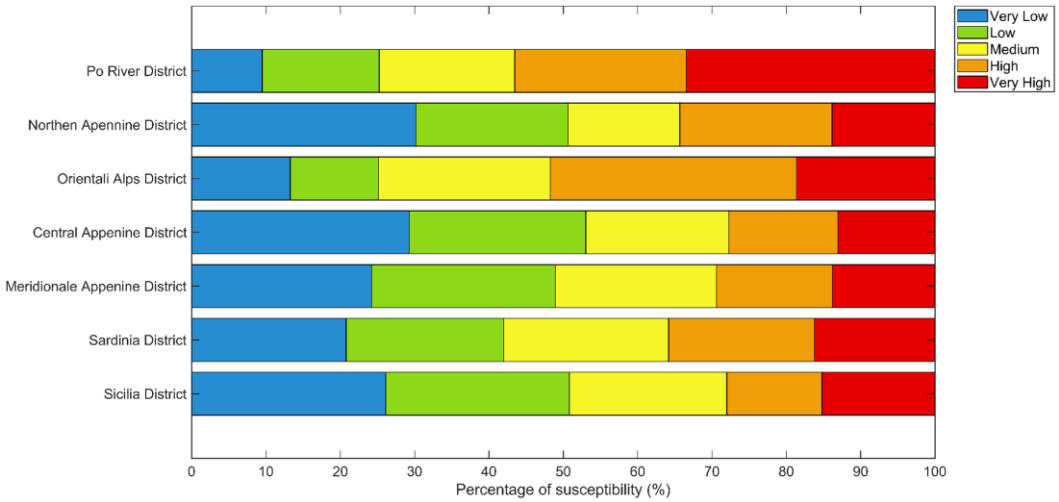

Figure 11. Percentage of Susceptibility Levels over the Main River Basin Districts existing in Italy.

A high flood risk is observed in the Po River District, where over 50% of the area falls into the high and very high susceptibility categories; this finding is consistent with its significant history of flood events. The Oriental Alps District shows a similar concentration of elevated risk, with over 50% of its territory also categorised as high and very high. These results align with the topographic and hydrological complexities of these regions, where steep slopes and flat floodplains coexist. In contrast, the Northern Apennine, Central Apennine, and Sicily districts show lower vulnerability, with more than 50% of their areas categorised as very low and low susceptibility.

These findings demonstrate clear regional variability in flood susceptibility, highlighting the need for district-specific risk management strategies. Nevertheless, this approach has shown an overestimation of the flooded areas.

The zoomed area of the Bradano basin is shown in Figure 12b and is compared with the Medium Probability Hazard flood map provided by ISPRA. A maximum flood water depth of 11.5m was estimated, where potential economic losses reached 1.8 and 3.6 million euros in industrial (27) and residential (992) buildings in the AOI, respectively. According to the agricultural land, the potential losses reached 3.6 million euros, affecting 6.1 km^2 (Figure 12).

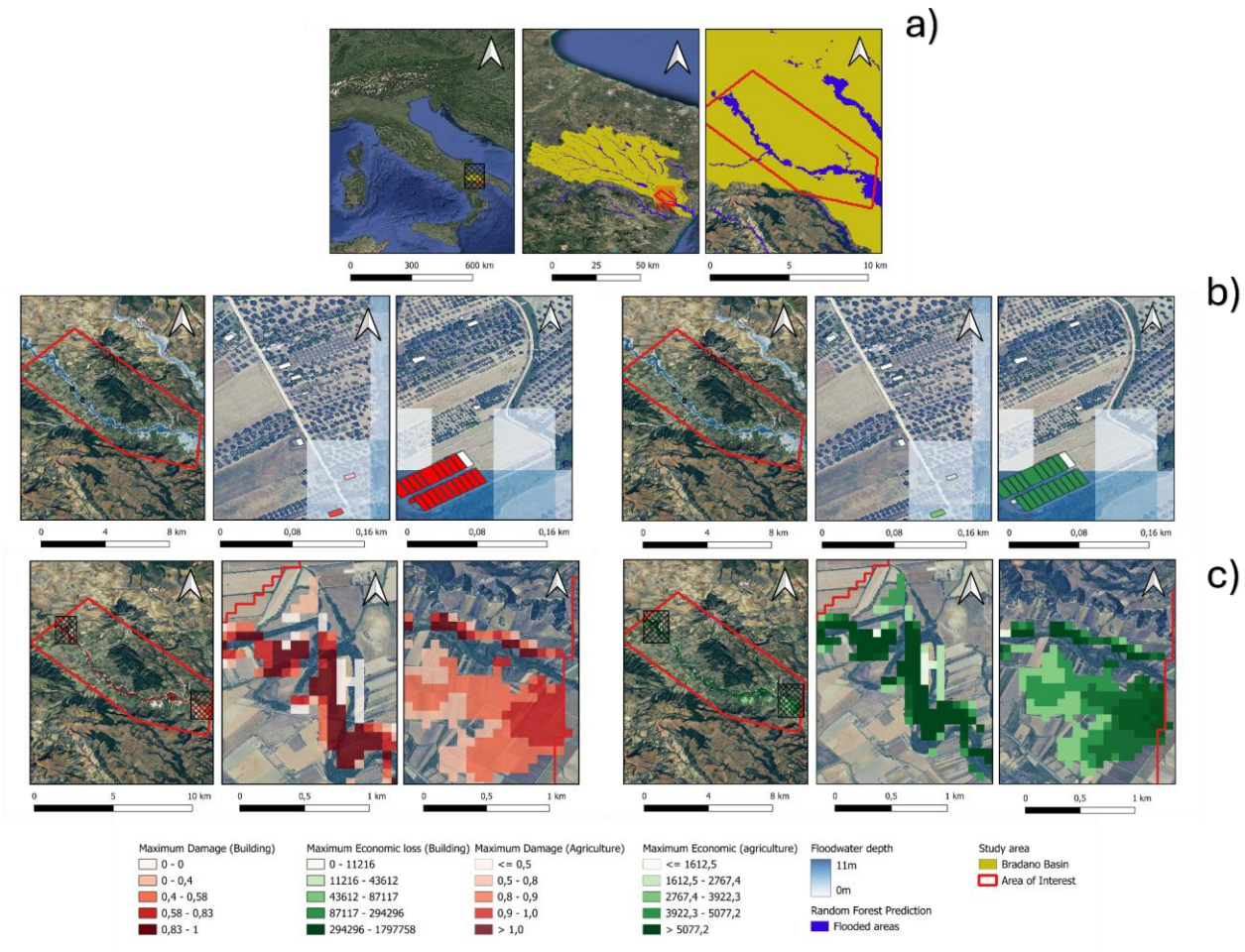

Figure 12. Flood damage analysis. a) Study area, AOI and flood-prone areas by the Random Forest model. b) Floodwater depth and building impacts. c) Agricultural land impact.

Future work will focus on refining exposure classification models, validating depth-damage functions for the Italian case, and incorporating additional socio-economic indicators to improve flood damage estimation. This study underscores the potential of data-driven methodologies to enhance flood risk assessment and damage evaluation. The results provide a basis for more effective risk management strategies and policy development in flood-prone regions.

Data-driven models that leverage observations, such as the one in this study, are proving invaluable for understanding the rapidly changing dynamics of local hydrological extremes. A critical direction for future research is assessing the transferability of these machine learning (ML) models to improve predictions in ungauged areas. Continuously refining susceptibility by mapping through such efforts is essential for informed decision-making, enabling proactive flood risk mitigation, strengthening environmental resilience, and safeguarding community well-being. However, those approaches have to be taken assuming a high uncertainty level, their results approximate the possible flood current conditions.

3.1.b.3 Probabilistic risk assessment for isolated areas in connection to riverine floods under evolving climate conditions

3.1.b.3.1 Methodological considerations

The methodological approach described in the first part of the deliverable (*DV 6.3.1 - Natural Hazards classification maps of individual network of linear infrastructures - Methodology Report*), was slighltly adjusted at the implementation phase. Below the main modifications are described.

The shortest path computation was modified since the application of the classical Dijkstra algorithm produced misleading results. A high degree of path overlap was observed among the derived shortest paths, which could introduce significant bias in the subsequent probabilistic risk modeling, particularly by overemphasizing frequently used network segments.

To address this limitation, for each origin–destination pair, a modified version of Yen's algorithm (Yen, 1971) was implemented. The revised procedure incorporates three key features: i) Bidirectionality, whereby for every traversed edge, both the u–v and v–u directions are considered when updating usage statistics and during path selection; ii) Incremental path removal, which forms the basis of Yen's algorithm and enables the extraction of successive shortest paths; and iii) a penalty-based edge weighting system.

The penalty mechanism discourages excessive reuse of the same segments by increasing the traversal cost of an edge proportionally to the number of times it has already been included in previously identified paths. Although Chondrogiannis et al. (2020) highlights potential limitations in the intuitive application of edge penalties, in this study –where origins typically represent spatially isolated locations– the generation of multiple, even slightly suboptimal, shortest paths remains valuable for probabilistic modeling.

By combining structural modifications (edge or node removal along root paths) with dynamic cost penalization, the proposed approach effectively yields a set of more diverse and realistic alternative routes for each origin–destination pair, thereby improving the robustness and representativeness of the network analysis.

Thus, we evaluate direct impacts to a given set of road links belonging to the k-shortest path between origin o and destination d, localized within a pertinence area x. This can be represented as $(\bar{P}_{o,d}^{k,x})_e$ where the set of road links is P, belonging to the k-shortest path between origin o and destination d, localized within pertinence area x is non-negligibly damaged by the event e. From this, the overall length of road links belonging to this sub-set can be indicated as $(\bar{L}_{o,d}^{k,x})_e$.

Considering these modifications, the isolation index can now be defined as:

$$II_o^e = \begin{cases} \dfrac{\sum_{x=1}^{X}\sum_{k=1}^{K}\sum_{d\in D}\gamma_{o,d}^{k,x,e}\cdot(\bar{L}_{o,d}^{k,x})_e}{\sum_{x=1}^{X}\sum_{k=1}^{K}\sum_{d\in D}\mu_{o,d}^{k,x,e}\cdot L_{o,d}^{k,x}} & if \sum_{x=1}^{X}\sum_{k=1}^{K}\sum_{d\in D}\mu_{o,d}^{k,x,e} > 0 \\ 0\ otherwise \end{cases} \quad (3.1.5)$$

The connection between o and d will be reduced according to the isolation index ratio, up to the extreme case where 100% of the k-shortest paths connecting o and d are no longer functional. Thus, the fraction of functional paths serves as an index of potential reachability (indirect impacts).

The inclusion of network-based analyses capable of capturing both direct and indirect impacts of flood events within a Probabilistic Risk Assessment (PRA) framework provides substantial added value. This integration extends the traditional scope of PRA –typically focused on physical damage– to also encompass functional disruptions, such as the isolation of critical locations due to infrastructure loss or inaccessibility.

Through this combined approach, it becomes possible to estimate classical risk metrics, such as the Average Annual Loss (AAL) and the Probable Maximum Loss (PML), within a network functionality context. Specifically, for this application, AAL and PML are computed at the origin level. The Isolation Index (II) is determined for each origin and each hazardous event: it provides the ratio of affected road length in all *k*-shortest paths in comparison to the total length of the *k*-shortest path for that origin. This value can be averaged over all simulated events providing information on the average annual Isolation Index for each origin. Similar estimates can also be derived for specific return periods, providing a means to identify those

origins most vulnerable to isolation. This allows for a more comprehensive understanding of network resilience, enabling decision-makers to identify critical nodes.

3.1.b.3.2 Case Study - an application to the Marche region

To realistically assess road network vulnerability to flooding, the Marche Region was selected as a case study, representing a diverse geographic and hydrological context in which flood hazards vary spatially across the terrain. The road network in this region is modeled as a graph directly reflecting the physical structure of paths and segments. Each edge corresponds to a road segment as mapped on the ground, enabling the simulation of flood impacts. This detailed representation is crucial given the spatial heterogeneity of floods, the number and their effects on individual infrastructure elements.

The road network for the Marche region was downloaded from OpenStreetMaps (through the OMSNx built-in functions in Python), counting more than 20 '000 segments and 13' 000 nodes, and more than 8 '500 km of road length (Figure 13).

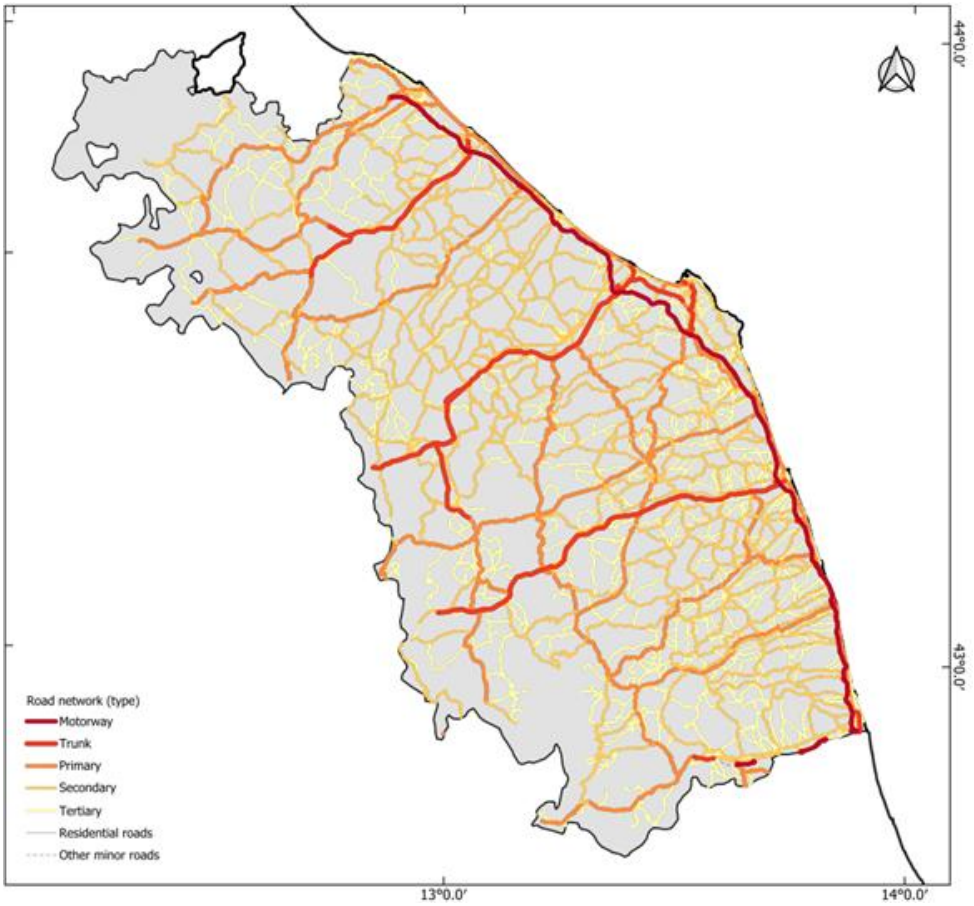

Figure 13. Complete road network for the Marche region (the road types included are motorway, trunk, primary, secondary, and tertiary).

The network incorporates road types from the Marche region corresponding to the following OpenStreetMap (OSM) highway categories: motorway, motorway_link, trunk, trunk_link, primary, primary_link, secondary, secondary_link, tertiary, and tertiary_link. A pre-processing analysis was conducted to evaluate and classify the importance of individual segments and nodes in terms of their connectivity and functional relevance within the overall network structure.

3.1.b.3.3 Model settings & parameters

The network graph is converted to an undirected type based on the assumption that, during flood emergencies, the road paths can be used in both directions for accessibility and evacuation. This assumption aligns with emergency management best practices allowed in different countries (e.g., Basalamah, 2020, Choe et al. 2023). Furthermore, parallel edges (i.e., multiple road segments between the same pairs of nodes) are retained -and not simplified- to account for the differential physical vulnerability of parallel routes to flooding, thus ensuring precise risk differentiation.

Should be noted that, since we are working in mountainous regions, many of the road segments may correspond to bridges or tunnels, which may or may not be affected by floods. However, due to the working scale, bridges and tunnels are considered as normal road segments.

To identify isolated locations, the top nodes ranked with the highest remoteness index values were identified as highly susceptible to isolation even in the absence of flooding or any external anomaly. A buffer of around each node is considered, to count the total population that lies within a 2 km ratio. The potential origins are identified as those nodes from the network that are intrinsically isolated and show less than 5,000 inhabitants in the tampon area. Based on these assumptions 16 origins were selected for this case study.

To identify service centers, hospitals are selected as the main destination points in the network, being among the most relevant critical facilities that can act as service providers in the context of emergencies. Thus, the objective will be to account for the ability of users located in isolated areas to reach any of these critical healthcare services during flooding conditions, or the opposite. A total of 20 hospitals -no matter their characteristics- are counted as destinations in the study area.

3.1.b.3.4 Implementation

Based on the selected origins and destinations, the calculation of a preliminary set of k-shortest paths is achieved using a version of the Dijkstra algorithm contained in the built-in OSMnx routing module in Python (ox.k_shortest_path). This function is efficient in terms of computation time and results, giving the very shortest and most efficient path. However, though assessing k-shortest path problems correctly, its "weight" parameter is limited. So, to address the issue previously introduced in the definition of the model (high degree of path overlap), a new script was implemented based on Yen's algorithm.

We developed an algorithm explained in the block diagram of Figure 14, that first computes the absolute shortest path using classical Dijkstra's algorithm (built-in in the NetworkX package in Python, nx_dijkstra_path), minimizing the sum of edge lengths between nodes (Figure 15). This step ensures that the optimal path is always captured before alternative routing options are explored.

After identifying the first path, each subsequent path is found by applying a modified version of Dijkstra's function by temporarily removing segments of already discovered paths. At the same time, incrementally edges that have been previously used are penalized by incrementing their weight by a given factor (these penalties are stored in a dictionary and call by the weight function parameter of the nx_dijstra_path function) (Akgun et al., 2000).

A comparison between the two different approaches is shown in Figure 15 and Figure 16. Comparing the shortest paths that connect a given origin (ID: 5253) with a given destination (ID: 8273) we observe minimum differences between the paths calculated with the first approach, while the modified algorithm is more efficient in finding alternative routes (Figure 15). On the other hand, Figure 16 shows the frequency distribution of the segments in the road network, and the number of times each segment is traversed by a shortest path. In average the algorithm used reduces the mean number of shortest paths traversing each segment from 90 times to 20 times.

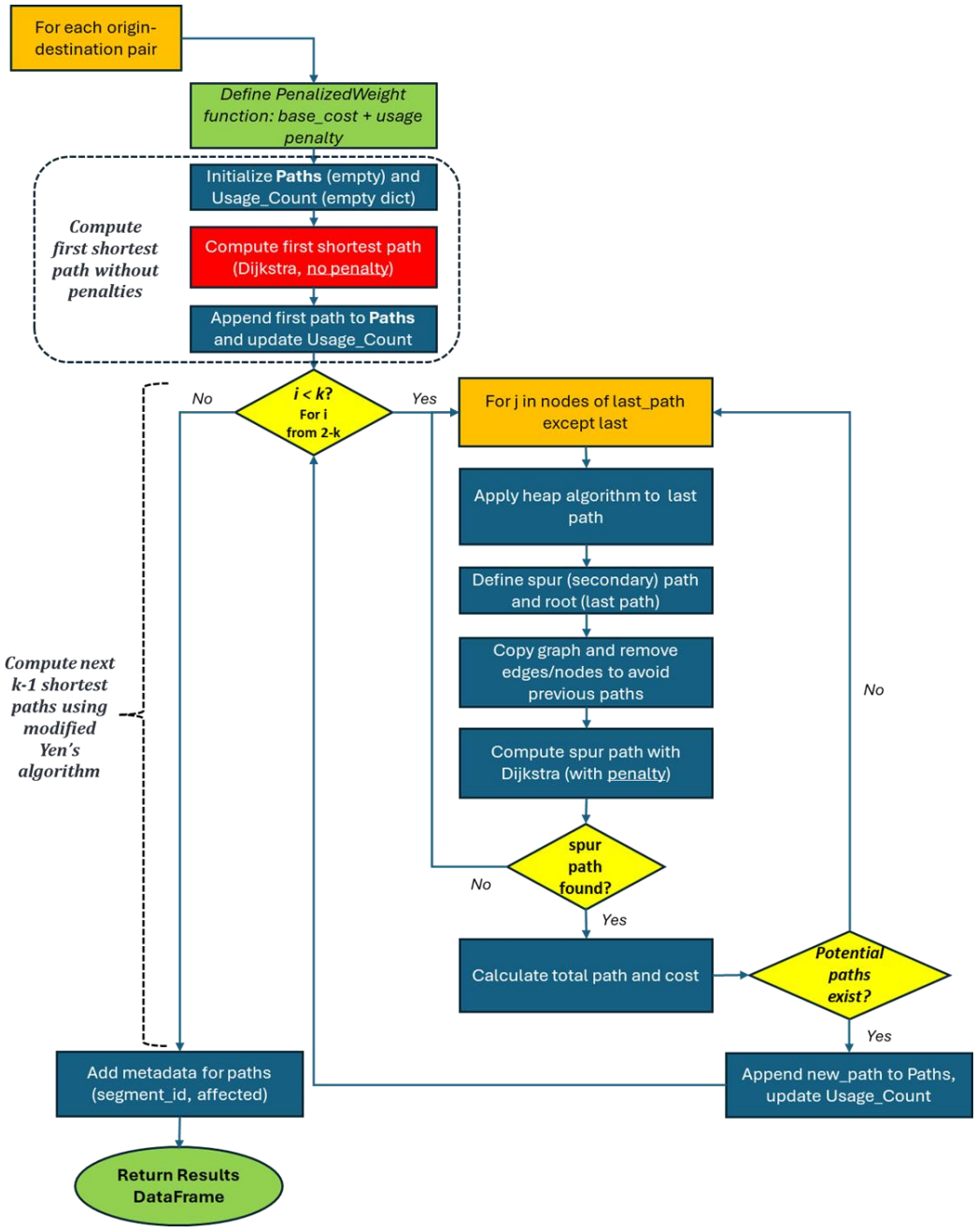

Figure 14. Block diagram summarizing the steps to compute k-shortest paths based on a modified version of Yen's algorithm with penalties.

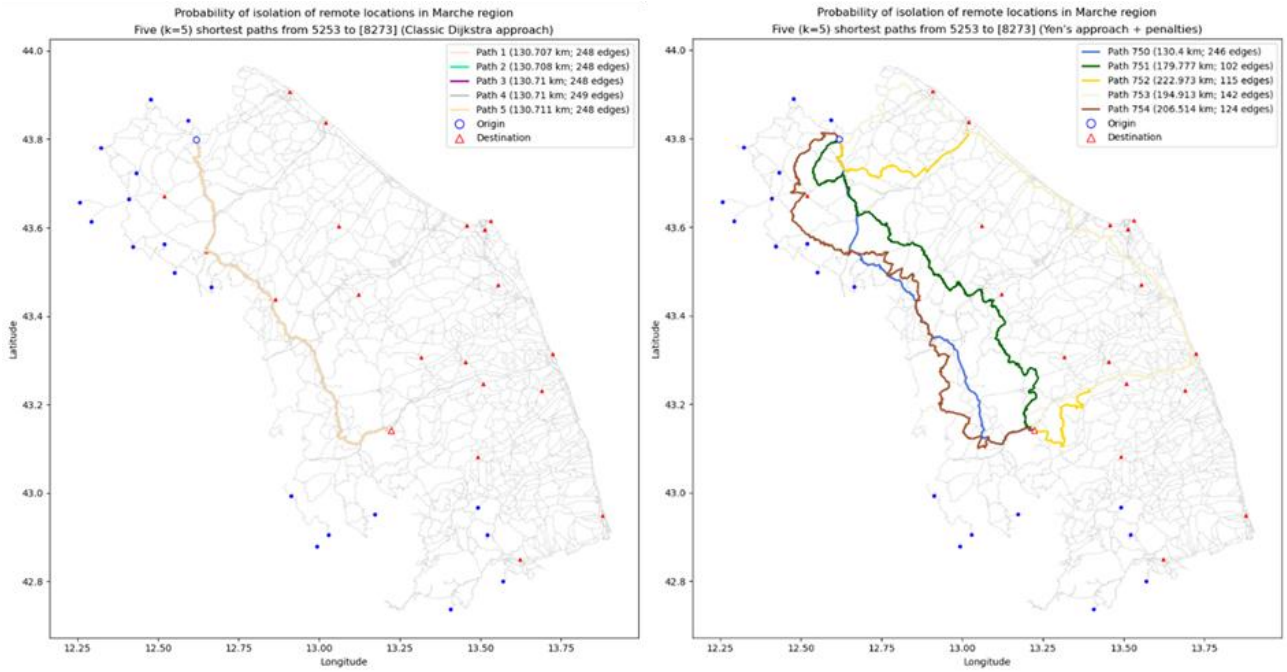

Figure 15. Example of variable shortest paths connecting one origin to one destination. Yet some segments are repeated, the algorithm manages to provide different paths to connect each origin-destination pair. In the approach followed (right) the first paths correspond to those calculated by classic Dijkstra algorithm.

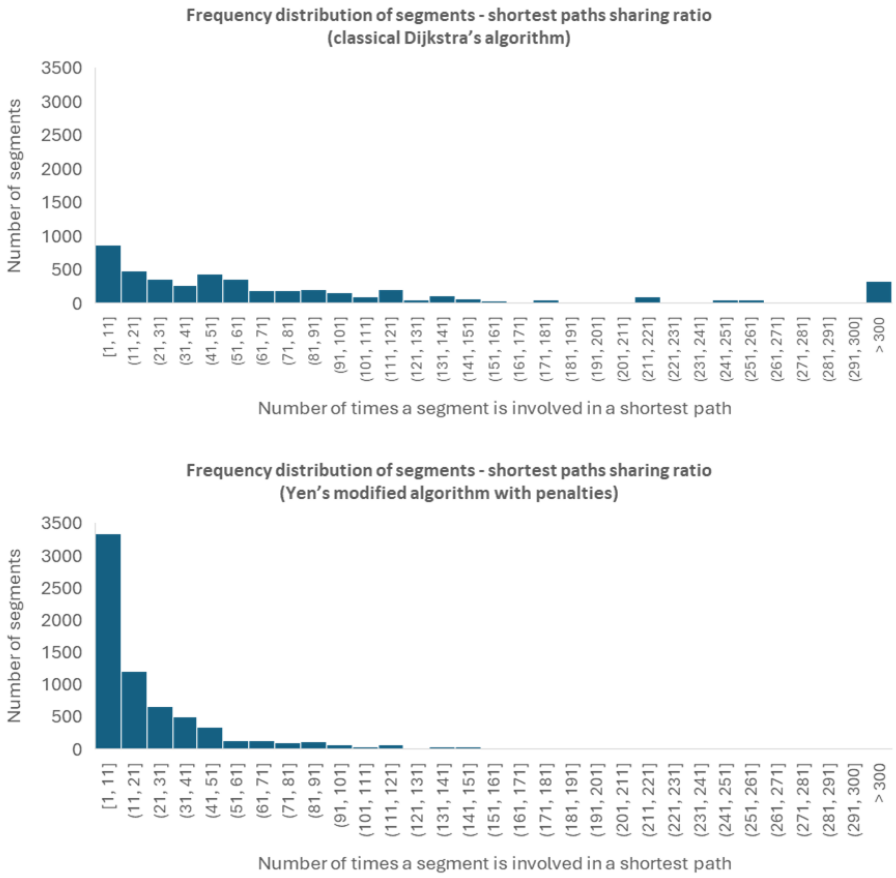

Figure 16. Frequency distribution of segments in the road network, according to the number of times each segment is traversed by a shortest path. Lesser segments are repeated with the second (bottom) approach.

The algorithm processes each origin saving the resulting shortest paths separately in .csv files. This chunk method helps to reduce the duration of each shortest path search loop (30 minutes per origin in our road network of ca. 20,000 edges). Once computed all origins, the chunks are aggregated, storing in a Pandas dataframe structure all the edges involved in the shortest paths, each one with a unique identifier (that relates them to each specific origin-destination paths) and all relevant metadata: the u and v endpoints, total path lengths, geometry and any additional network attributes (i.e., street names).

The network containing only edges (as polyline features) involved in any shortest path is trimmed by the hydrological watersheds. In particular, a total of 3,515 road segments were selected to be used as input data for the PRA. These segments correspond to the portion of the road network that intersects the 1000-yr return period flood hazard map and that are involved in at least one shortest path. This trimmed network is rasterized to be used as input of the Probabilistic Flood Risk Assessment (PRA) using the same pixel size as the hazard component (Figure 17).

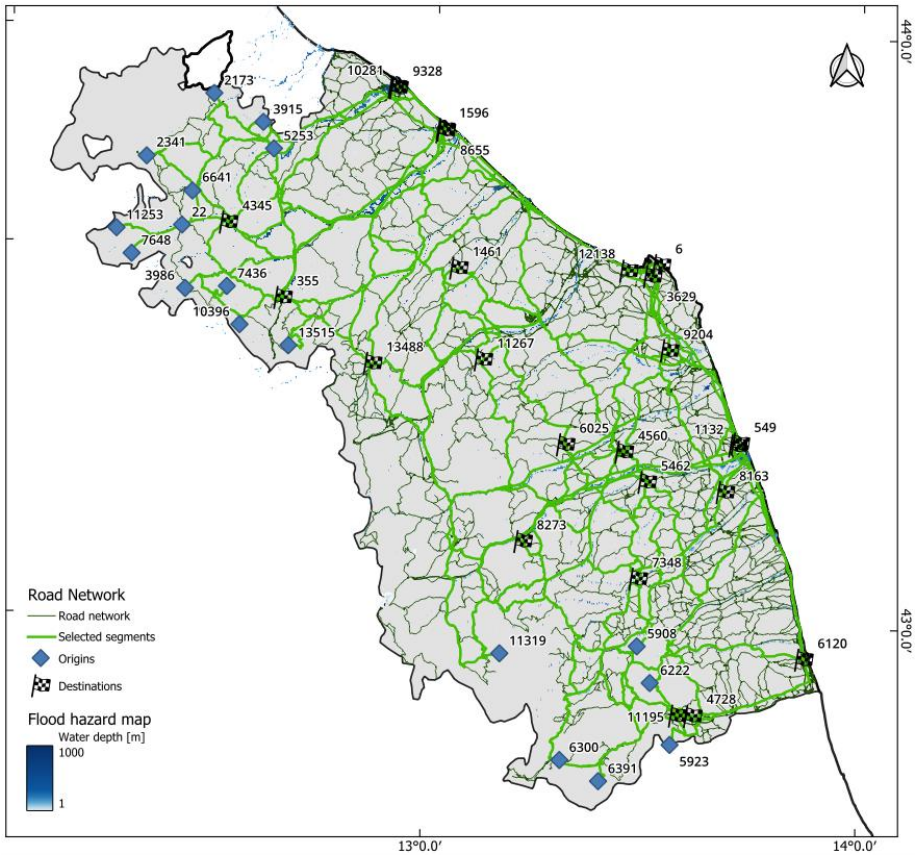

Figure 17. Origin and destination points and trimmed road network with selected edges used as input data for the PRA modelling stage. In background the 1000-years flood hazard map is shown as reference.

To support the post-PRA processing, a mapping table is created, relating each network arc (with a unique identifier) with the k-shortest paths that traverse it and, therefore, all the origin-destination pairs that are connected through those segments (Figure 18).

feature_id	basin_id	segment_id	geometry
1	651	17	line (...)
2	666	17	line (...)
3	669	10	line (...)
4	674	16	line (...)
5	676	2401	line (...)
6	679	0	line (...)
7	651	20	line (...)
8	651	21	line (...)
9	651	24	line (...)
10	651	25	line (...)

segment_id	od_paths
0	[1560, 1561, 1562, 1563, 1564, 1565, ..., 1769, 1790, 1791, 1792, 1793, 1794]
1	[1560, 1561, 1562, 1563, 1564, 1565, ..., 1769, 1790, 1791, 1792, 1793, 1794]
3	[1600, 1601, 1602, 1603, 1604, 1605, 1606, 1607, 1608, 1609, 1610, 1611, 1612, 1613, 1614, 1615]
5	[1560, 1561, 1562, 1563, 1564, 1565, ..., 1675, 1676, 1677, 1678, 1679, ..., 1790, 1791, 1792, 1793, 1794]

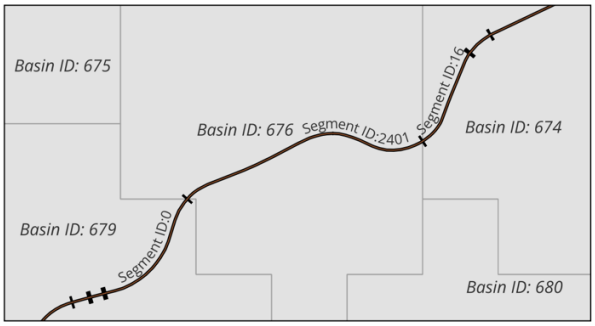

od_path	origin	destination	k_path
1555	3915	4345	1
1556	3915	4345	2
1557	3915	4345	3
1558	3915	4345	4
1559	3915	4345	5
1560	6391	11267	1
1561	6391	11267	2
1562	6391	11267	3
1563	6391	11267	4
1564	6391	11267	5

Figure 18. Main tables used for the process of the results of the Probabilistic Risk Assessment.

The methodology for scenario generation, briefly introduced in the modelling chapter, was applied to the Marche region to simulate 3,000 years of potential flood events (approximately 15000 events) affecting different areas of the domain with varying intensities. The discharge data used as input for scenario generation are those described in Bruno et al. (2021). Each event, characterized by water level at 5 m resolution in the affected areas, was processed by the risk calculation engine that provides, as direct output, the number of pixels in each road segment affected by a water level above 50 cm.

During the post-processing stage, the pre-compiled mapping table allows to define which shortest paths are disrupted due to direct impacts on specific road segments. For each origin point and each simulated event, the proportion of affected roads within all shortest paths (as the ratio of pixels affected/pixels exposed), as well as the overall length of those paths, are calculated to derive the Isolation Index.

During the post-processing stage, the Isolation Index values were used to compute conventional risk metrics, specifically the Annual Average Loss (AAL) and Probable Maximum Loss (PML) for each origin. Finally, tables and maps were generated to visualize the impacts of flooding on the road network.

3.1.b.3.5 Results

From the total set of events, a random subset is shown in Figure 19, depicting how the affection of different segments in the road network can have an impact on the accessibility to different locations (origins).

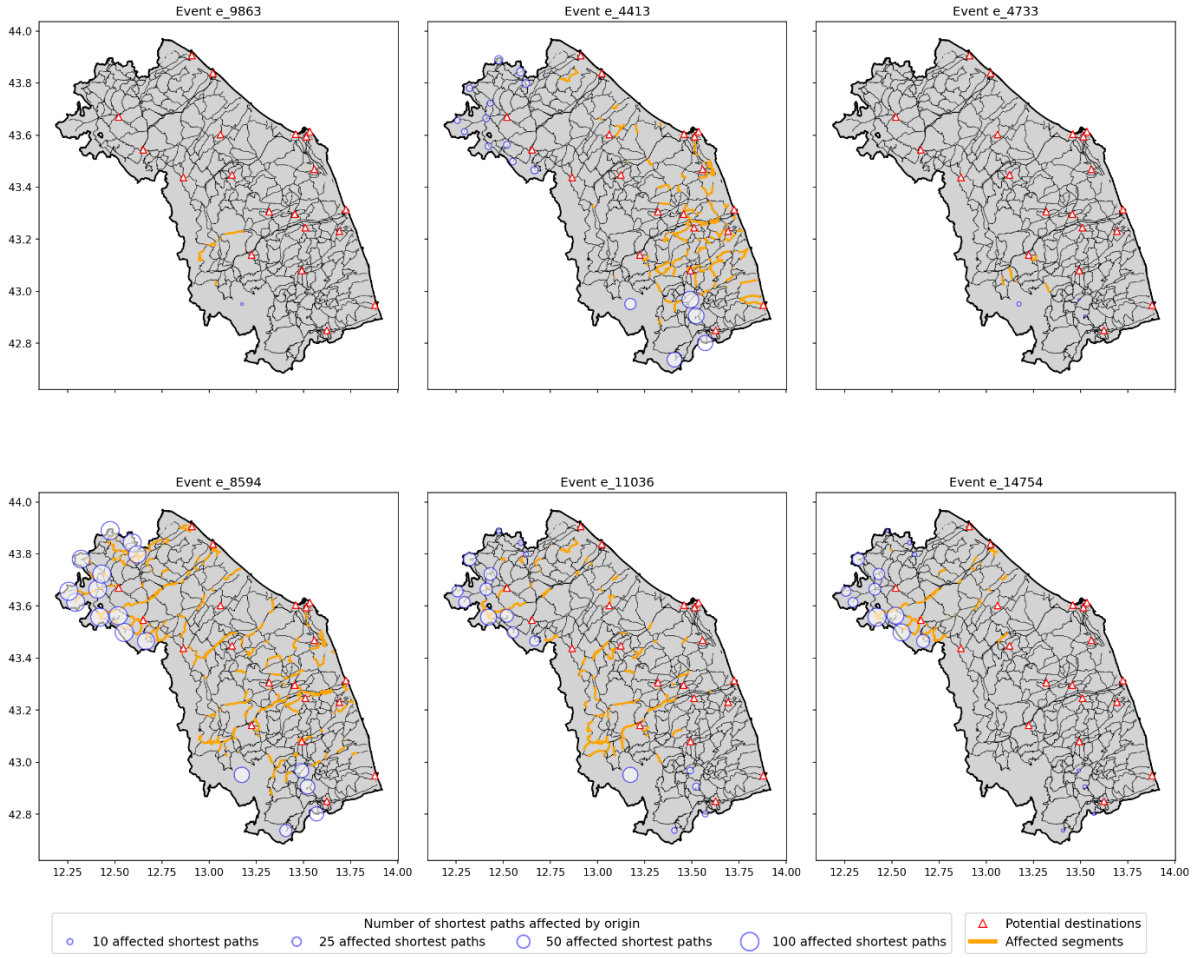

Figure 19. Random subset of events depicting the frequency of shortest paths affected per event.

Six maps for the Marche region, each corresponding to a different simulated flood event (Event e_9363, e_4413, e_4733, e_8394, e_11035, e_14754) are shown in Figure 19. On each map, the road network and the set of origin points are shown, with roads affected by flooding highlighted in orange. In addition, for each origin, the number of shortest paths impacted by that specific flood event is shown. The figure visually conveys the spatial distribution of flood impacts on the road network and how these impacts vary by event. In some events (e.g., e_8394), many origins experience widespread interruptions of their shortest paths (more and larger circles), whereas other events (e.g., e_9363) show more localized impacts.

The maps show that the impact of flooding on connectivity is highly event-dependent. Some events affect numerous shortest paths from multiple origins, while others are more localized: these maps highlight the importance of an analysis that takes all possible events into account to properly assess risk of isolation.

Hence, we computed AAL and PML for each assigned return period considering the impact at origin level as the ratio between the total number of pixels of road segments affected per event and the total pixel count representing the total road segments length associated to each origin for all events.

Each panel in Figure 20 represents the spatial distribution of the isolation index for isolated communities (origins) toward hospital destinations in terms of annual loss and for two different return periods. The three maps use the same base layers: the modeled road network (motorway, trunk, primary, secondary, tertiary roads); the hospital locations (as service centers or destinations); and the isolated origin nodes. The points used as origins (i.e., intrinsically remote locations) are coloured according to the percentage of shortest paths disrupted by flooding (i.e., the isolation index)

The isolation index quantifies the proportion of affected paths (Figure 20). The annual average results do not reveal any prominent hotspots: most origins show an isolation index ratio of approximately 0.4–0.5%. However, when focusing on higher return periods, it becomes evident that origins located in the northern

part of the region are more severely impacted by road flood disruptions than those in the south. This finding highlights the need for targeted mitigation strategies and infrastructure reinforcement in the most vulnerable northern areas to enhance regional resilience and maintain equitable access to essential health services.

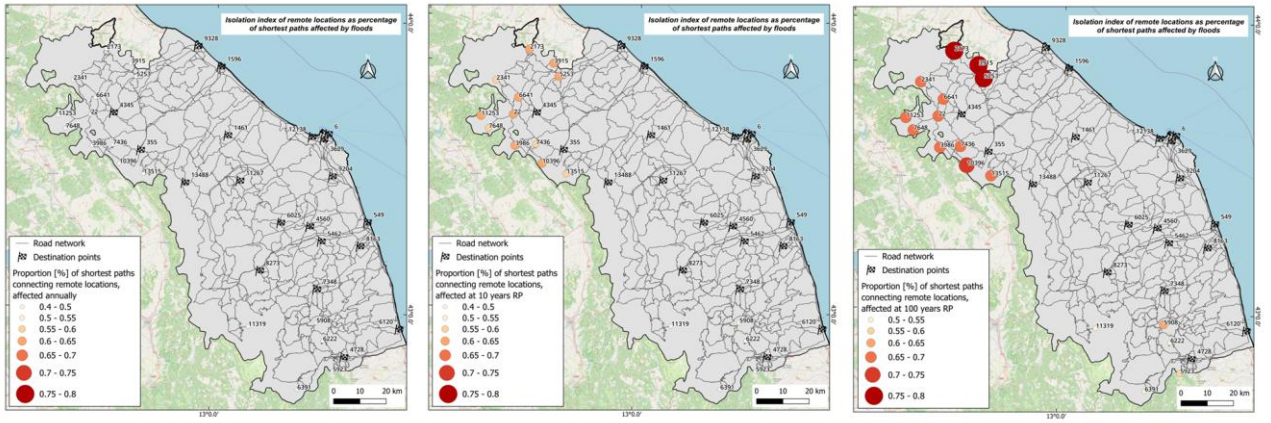

Figure 20. Isolation Index results for each origin, shown as the annual average (left), and for two return periods—10 years (center) and 100 years (right).

Last, the PML curves were calculated to relate the percentage of total shortest paths affected to the return period in years. Each curve in Figure 21 corresponds to one of the selected origin nodes (isolated locations) in the Marche region, and shows how the isolation index changes (the proportion of connectivity loss to any service center). Most curves rise sharply between 2 and 25 years, indicating that a large share of road access routes can be disrupted with relative high frequency. Beyond approximately 50 years, curves tend to stabilize or plateau. These curves highlight network fragility concentrated in a few critical edges; the spatial differentiation among curves suggests the need for site-specific mitigation: improving alternate access for the most sensitive origins rather than uniform interventions.

These PML curves provide a quantitative basis for prioritization: origins with the steepest curves should be considered high-risk isolation hotspots. The curves also serve as probabilistic indicators of accessibility loss, suitable for integration into regional-scale flood risk models or infrastructure resilience assessments.

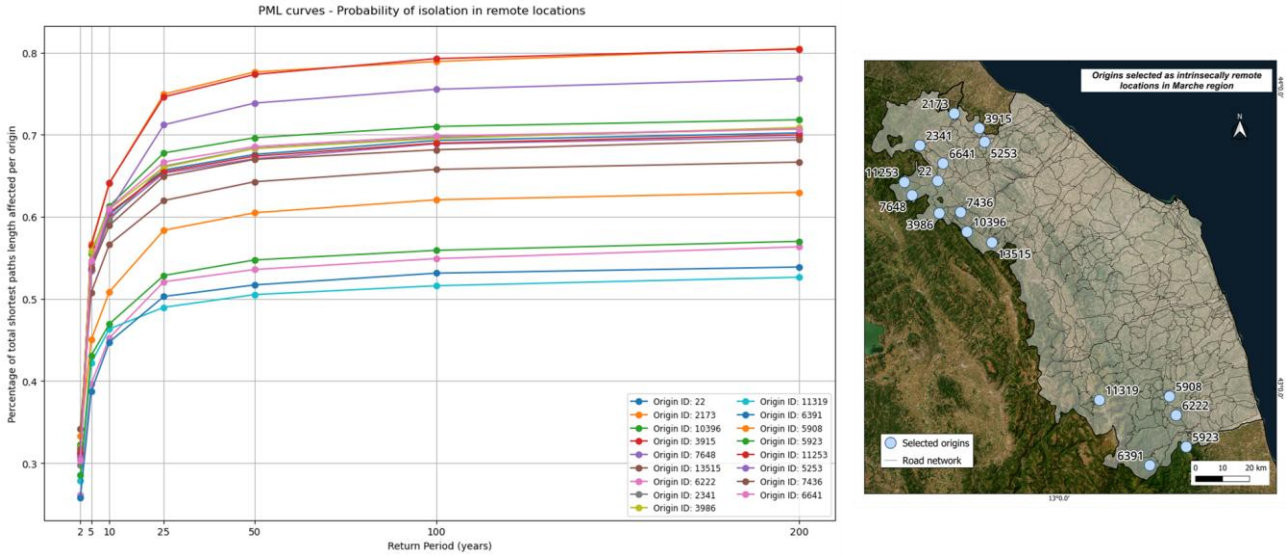

Figure 21. Probability of isolation (PML curves) for remote origins in the Marche region as a function of return period. A map with the origins locations is shown to the right.

3.1.c Mapping of coastal flooding induced by extreme wind waves

3.1.c.1 MeteOcean Data

The work integrates in-situ and satellite observations, numerical modelling, data calibration, and statistical analyses to establish a robust framework for understanding wave dynamics and their projected evolution under future climate scenarios. The initial phase of the project focused on the acquisition and analysis of wave measurements from the *Italian National Wave Measurement Network* (ISPRA, *Italian National Wave Buoys Network* – RON). Historical buoy records were processed to characterize the local wave climate, including significant wave height, wave period, and direction, as well as the statistical distribution of extreme events. These direct observations were complemented by satellite-derived datasets from the *ESA SeaState* project, offering an extended spatial perspective on offshore wave conditions. The combined use of buoy and satellite observations provided a comprehensive reconstruction of the marine climate across the study area, forming a solid empirical basis for the subsequent modelling and calibration phases (see Deliverable 6.3.1 – Methodological Report for further details).

Building on the observational datasets, the subsequent phase focused on generating long-term wave time series through numerical modelling. The ERA5 reanalysis, produced by the *European Centre for Medium-Range Weather Forecasts*, was employed to reconstruct historical wave conditions from 1979 to 2024. In parallel, future wave projections were obtained from the *Copernicus Climate Data Store*, which provides climate scenario simulations under two *Representative Concentration Pathways* (RCPs): RCP4.5, representing a moderate-emissions pathway assuming effective mitigation policies, and RCP8.5, a high-emissions "business-as-usual" scenario characterized by continued growth in greenhouse gas concentrations.

3.1.c.2 Case Study Overview

The study focused on the analysis of a representative coastal area along the Tyrrhenian coast, selected as a pilot site for the evaluation of wave climate and coastal hazard conditions. The area is characterized by sandy shorelines and the presence of major coastal infrastructures, making it particularly sensitive to marine forcing and extreme events such as erosion and flooding.

3.1.c.2.1 Calibration of the model data and definition of offshore extreme conditions

The first phase of the study was dedicated to the acquisition and processing of in-situ wave measurements from a buoy of the RON network. Historical data were analyzed to describe the local wave regime in terms of significant wave height, period, and direction, as well as to estimate the statistical distribution of extreme events. These measurements were complemented by satellite-derived data from the *ESA SeaState* project, which provided a broader spatial perspective on offshore wave conditions. The integration of buoy and satellite observations enabled a comprehensive reconstruction of the regional marine climate, forming the basis for subsequent modelling and calibration activities. Model outputs were extracted at multiple grid points progressively offshore from the reference buoy, in order to assess the influence of coastal proximity and offshore variability. Statistical analyses confirmed the predominance of western wave directions and significant wave heights generally below five meters, with extreme events reaching up to about eight meters for the highest return periods. These results established a reference framework for the following calibration and validation phases.

Model-based time series of sea states often present systematic deviations from observed data, mainly due to limitations in model resolution, atmospheric forcing, and boundary conditions. To reduce these discrepancies, a dedicated calibration methodology was developed, combining bias correction and multivariate analysis techniques. The calibration was based on the comparison between modelled and observed wave parameters, including significant wave height, period, and steepness, and was designed to improve both accuracy and temporal consistency. Different correction strategies were tested, from simple univariate approaches to more advanced multistep formulations that account for evolving sea-state conditions. The resulting calibrated time series constitute a homogeneous and high-quality dataset suitable for advanced statistical analyses.

Building on the corrected model data, the subsequent phase of the work focused on the statistical characterization of extreme wave conditions. The objective was to define representative offshore design parameters and to assess their potential evolution under changing climatic conditions. Both stationary and non-stationary approaches were employed, applying Generalized Extreme Value (GEV) models to long-term time series of significant wave height. The non-stationary framework allows key distribution parameters to vary over time, thus capturing potential trends and long-term shifts in the wave climate.

This methodology enables the estimation of design wave heights associated with specific return periods (e.g., 50 or 100 years) at any point in time, providing a dynamic perspective on how marine hazards may evolve throughout the century. Results generally indicate that under high-emission scenarios, extreme wave conditions may intensify, whereas moderate-emission pathways lead to more stable or slightly decreasing trends. These findings highlight the importance of integrating non-stationary statistics into coastal design and adaptation strategies. Overall, this integrated framework, combining data calibration and statistical inference, provides a consistent approach for the definition of offshore extreme conditions. The results form a methodological foundation for the assessment of future marine hazards and for the design of resilient coastal and port infrastructures.

3.1.c.2.2 Propagation of Offshore Extreme Waves, Run-Up Estimation, and Coastal Flood Mapping

The analyzed coastal area represents a representative example of a low-lying Mediterranean shoreline exposed to storm-induced erosion and flooding. The combination of narrow beaches, limited sediment supply, and the presence of critical coastal infrastructure makes this type of setting particularly sensitive to marine forcing. Increasing storm frequency and intensity, together with sediment imbalance and the widespread use of hard coastal structures, have intensified erosion processes and shoreline retreat in recent decades.

To simulate wave transformation from offshore to nearshore, a two-dimensional hydrodynamic modelling framework was implemented using the MIKE 21 model (provided by DHI company), a well-established tool for the simulation of coastal wave propagation. The computational domain was discretized with an unstructured triangular mesh featuring variable resolution, with higher spatial detail in the nearshore zone to accurately reproduce wave transformation processes such as refraction, shoaling, and breaking. Bathymetric data up to the –20 m isobath were reconstructed by integrating multiple datasets (C-MAP Professional+, EMODnet Bathymetry), interpolated to obtain a high-resolution digital bathymetric model. Extreme wave conditions were propagated across the domain to assess nearshore wave energy distribution and potential inundation extents.

Run-up parameter was estimated using several empirical formulations available in the literature (Holman, 1986; Mase, 1989; Ruggiero et al., 2001; Stockdon et al., 2006; Nielsen, 2009; Vousdoukas et al., 2012; Poate et al., 2016; Atkinson et al., 2017), which relate run-up levels to wave characteristics and beach slope. Among these, the Stockdon et al. (2006) formulation was selected for the production of coastal flooding maps, given its robust empirical validation and widespread application in coastal hazard assessments.

To accelerate the estimation process, a multilayer perceptron (MLP) neural network model was trained using the Stockdon run-up outputs, enabling rapid prediction of run-up values from basic wave parameters. The model achieved high accuracy (R^2 up to 0.98) and low errors, confirming the effectiveness of integrating numerical modelling with machine learning for fast and reliable coastal hazard assessment. Results from the numerical simulations and empirical calculations revealed the spatial variability of run-up and inundation potential along the coastline. The comparison between return periods of 5 and 500 years highlights a substantial increase in inundation extent and hazard intensity under extreme conditions, with critical sectors emerging where local morphology amplifies wave run-up and overtopping processes. These areas represent priority zones for targeted coastal management, continuous monitoring, and the design of adaptive protection measures.

The combination of wave propagation modelling, empirical run-up estimation, and data-driven predictive tools provides an integrated framework for coastal flood hazard mapping. This approach supports decision-making for coastal risk management, contributing to the broader objectives of the RETURN project by promoting climate-resilient planning and sustainable coastal protection strategies.

3.1.c.2.3 Access to Results and Data Availability

The detailed results, including complete datasets, model outputs, and high-resolution flood maps, are stored within the project's digital repository. Access to the full documentation and extended analyses is granted to authorized members of the RETURN partnership through the dedicated *SmartBox* platform within the POC system, under a full privacy and restricted-access setting.

External access to the data and results can be provided upon formal request, subject to project data-sharing policies and confidentiality requirements. Summary results and methodological overviews are available within this report, while the complete database remains reserved for internal project use and research validation activities.

3.1.d Enhanced methodologies of landslide hazard assessment over network legs

3.1.d.1 Introduction

Landslides are complex natural phenomena that pose severe geohazards in many countries, occurring in diverse geological, geomorphological, and climatological environments. Thus, understanding the spatial and temporal distribution of landslides is crucial to assess related hazards and to support a comprehensive risk assessment (Grelle et al, 2014; Fusco et al, 2023). The growth of urban settlements has led population settlement in areas at risk, where prediction and prevention actions are nowadays a challenge for geoscientists. In this context, landslide inventories can be used for various purposes, such as: preliminary steps for the assessment of landslide susceptibility, hazard and risk. They are valuable for investigating landslide distribution, types and patterns in relation to morphological and geological factors as well as for studying landscape evolution. However, the practical utility of these inventories is often constrained by limited accessibility, spatial inhomogeneity, or use of different mapping methods and classification criteria. This condition stands as a significant limitation for studies aimed at landslide susceptibility and risk assessment.

Landslide susceptibility assessment is the most common approach to assess how prone to landsliding is a landscape. Several methods and approaches, both qualitative and quantitative, have been proposed and tested for distributed landslide susceptibility assessment (Reichenbach et al, 2018). Assuming that "the past is the key to the future" (Carrara et al, 1995), the model learns how to distinguish the presence from the absence of a landslide based on a set of predisposing factors (i.e. slope degree, curvature, aspect, geology). The model performance has significantly improved in the last decade, particularly with the emergence of artificial intelligence-based models (Dahal & Lombardo, 2023). Unfortunately, only a small portion of those, called explainable AI, gives the user the possibility to fully understand the result. Therefore, in this work we preferred to use a fully interpretable statistical model, the Generalized Additive Model (GAM) to perform, not only, a landslide susceptibility analysis but also to estimate the landslide intensity which indicates the level of threat associated with the event (Titti et al, 2025; Lombardo et al, 2021).

The analysis has been conducted in Calabria region, in the context of the Proof Of Concept 1 selected by the Spoke TS2 to evaluate potential interactions between natural hazards and linear infrastructures.

3.1.d.2 Collection and homogenization of available landslide inventories

Landslide inventory is the most important data required by data-driven models. To perform susceptibility and intensity analysis, the minimum requirement is the availability of a polygonal landslide inventory in the study area. In Calabria region three compatible landslide inventories are available: IFFI (Triglia et al., 2010), CaLaI (Cianflone et al., 2025), and the events collected by the local authorities.

In Italy, many studies have already been conducted to map landslide susceptibility both at the basin scale and, less frequently, at the national scale. Among these, one of the most recent studies is the one presented by Loche et al. (2022). The aim of the study is to determine landslide susceptibility at the national scale for each type of landslide present in the territory, using a statistical methodology (Generalized Additive Model - INLA) based on the IFFI inventory. They highlighted a lack of homogeneity in the spatial distribution of events at national scale. This allowed them to identify regions with more detailed inventories compared to others respecting the single type of landslide indicated by the inventory. Referencing to the Calabria region, the landslide types indicated to be used as training dataset are: complex, DSGSD, shallow, rotational/translational slide.

This work is part of a multi-step analysis carried out in collaboration with the Spoke VS2 together with whom we defined the landslide classification to be used in the analysis. Therefore, considering the project context and the consideration of Loche et al. (2022), the analysis presented in this work has been performed grouping complex and rotational/translational slide from the IFFI inventory in Calabria region. DSGSD and shallow landslide have been excluded from the analysis because their density was to low to be used in a statistical model.

Overall, 8067 complex and rotational/translational slide have been considered, numbered in 2512 Slope Units (SU) delineated by Alvioli et al. (2020) over a total of 17106 SU (15%) with an average area of 660165 m2 (Figure 22). The number of SU doesn't include the green area called 'Transfer area' in Figure 22A. That portion of region has been excluded from the training dataset because the landslide inventory has been collected starting from populated areas, thus the 'Transfer area' suffers a lack of landslide information. The 'Transfer area' has been delineated by a kernel density operation with 5km of radius.

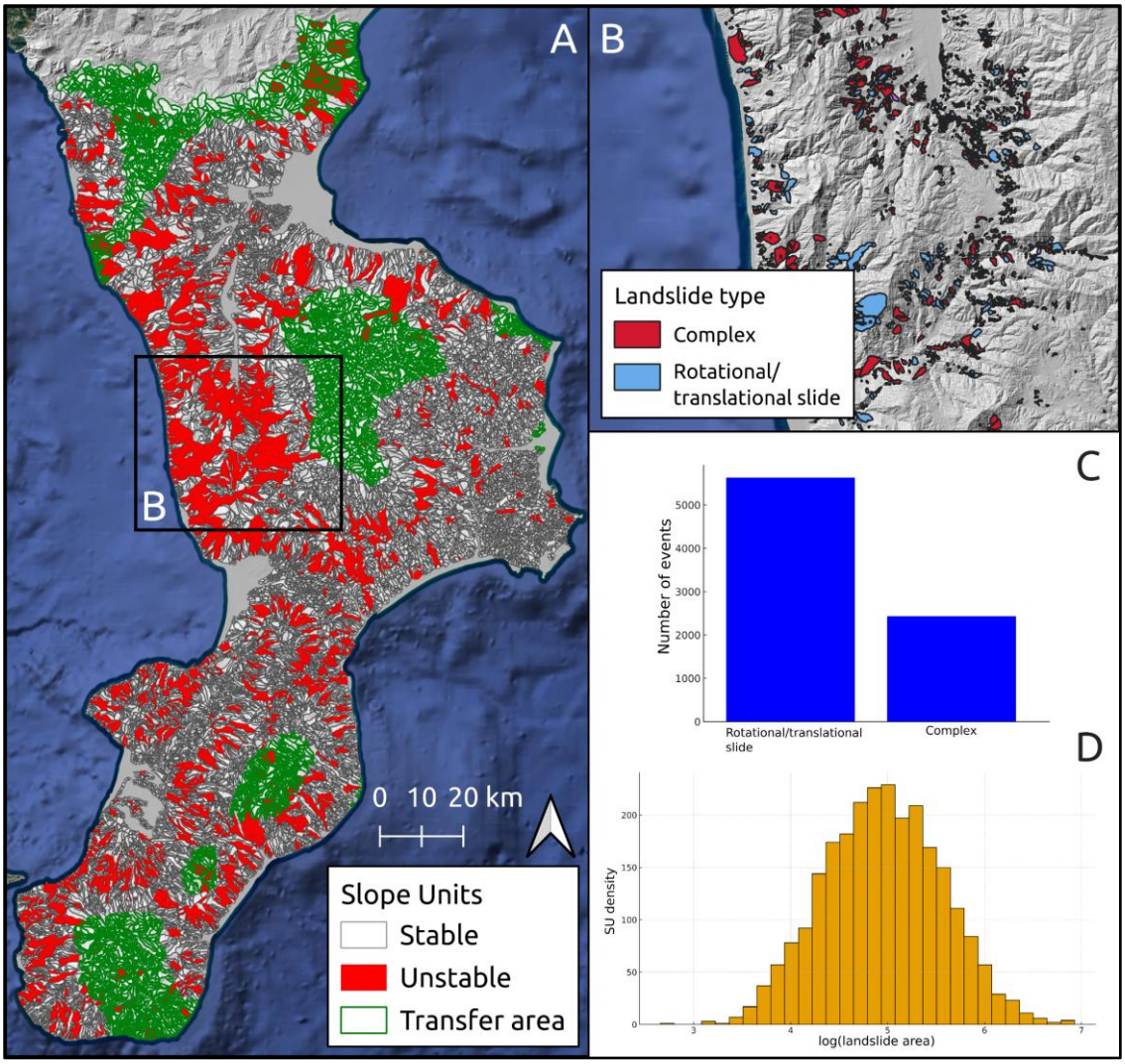

Figure 22. A - Landslide distribution in SU delineation. The Transfer area is the one excluded by the training dataset. B – Zoom on the landslide polygons. C – Grouped landslide types. D – Distribution of the landslide area per SU.

3.1.d.3 Landslide susceptibility assessment and intensity evaluation

To perform the landslide susceptibility and intensity first we calibrated the model selecting the explanatory variables (covariates hereafter) collected from different sources: the morphological variables have been derived from the DEM Copernicus GLO-30, rainfall data from dataset published by Gariano et al. (2015), temperature from MODIS, land cover from CORINE LAND COVER (https://doi.org/10.2909/71c95a07-e296-44fc-b22b-415f42acfdf0) and lithology from Calabria region (https://geoportale.regione.calabria.it/). The estimation of landslide susceptibility and intensity has been conducted using the GAM model implemented in the SZ-plugin (Titti et al., 2025). The former solves binomial likelihood, it is a binary classification problem based on the landslide presence/absence; The latter solves Gaussian likelihood, it is a regression problem based on the landslide area. All the covariates have been used as non-linear effect: mean of slope, mean of profile curvature, mean of tangential curvature, mean of yearly cumulative rain, standard deviation of yearly cumulative rain, mean of yearly mean temperature, mean and standard

deviation of yearly mean NDVI, mean and standard deviation of elevation. Only one has been used as linear effect: mean of distance to stream. The others as categorical: land cover and lithology. Mean and standard deviation are referred to the spatial distribution of the covariate in each SU.

The classification model has been trained on the SUs that are shown in Figure 22A colored red and white and predicted on the green SUs in Figure 22A. However, the regression model has been trained where the landslides are present (Figure 22A stable SU), considering the cumulative area of all the landslides in each SU where the landslides were activated, and predicted in the rest of the SUs. The initiation points have been defined considering the 90esimo percentile of the landslide elevation pattern. All the models have been cross-validated using 10-fold random cross-validation and 10-fold spatial cross-validation. The classification model has been evaluated using AUC, F1 score (F1) and Choen's Kappa (K), whereas the regression model has been evaluated comparing the predicted results and observed data through Mean Absolute Error (MAE), Root Mean Square Error (RMSE), squared R (R2) and Pearson Correlation Coefficient (PCC).

The results of the susceptibility and intensity assessment have been shown in Figure 23 and Figure 24, respectively. Both maps show elevated values of landslide probability and predicted landslide area along the Tirranean cost. Overall, the metrics of the susceptibility show a quite high prediction capacity of the model in Figure 23. Nevertheless, the confusion matrix based on the Youden index cutoff reveals that 78% of the unstable SU have been predicted correctly (true positive). After several considerations and alternatives to reduce the number of false negative, we can say that the goodness of the analysis is limited by the quality of the landslide inventory as also confirmed by the metrics of the intensity model which are quite poor (Figure 24). Unfortunately, a comparison with the results published by Loche et al. (2022) is impossible due to the different landslide classification used.

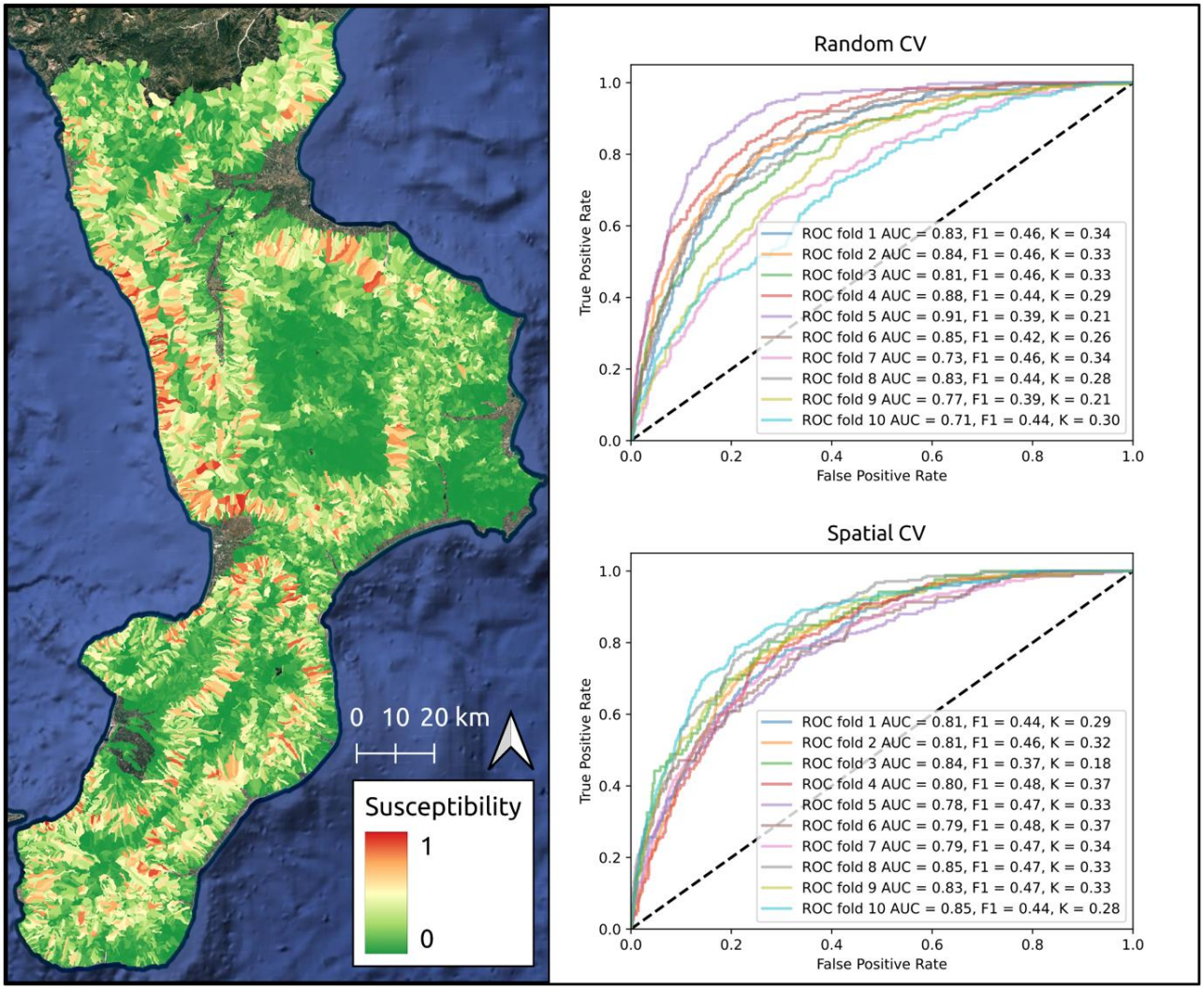

Figure 23. Landslide susceptibility map and the relative random and spatial cross-validation metrics.

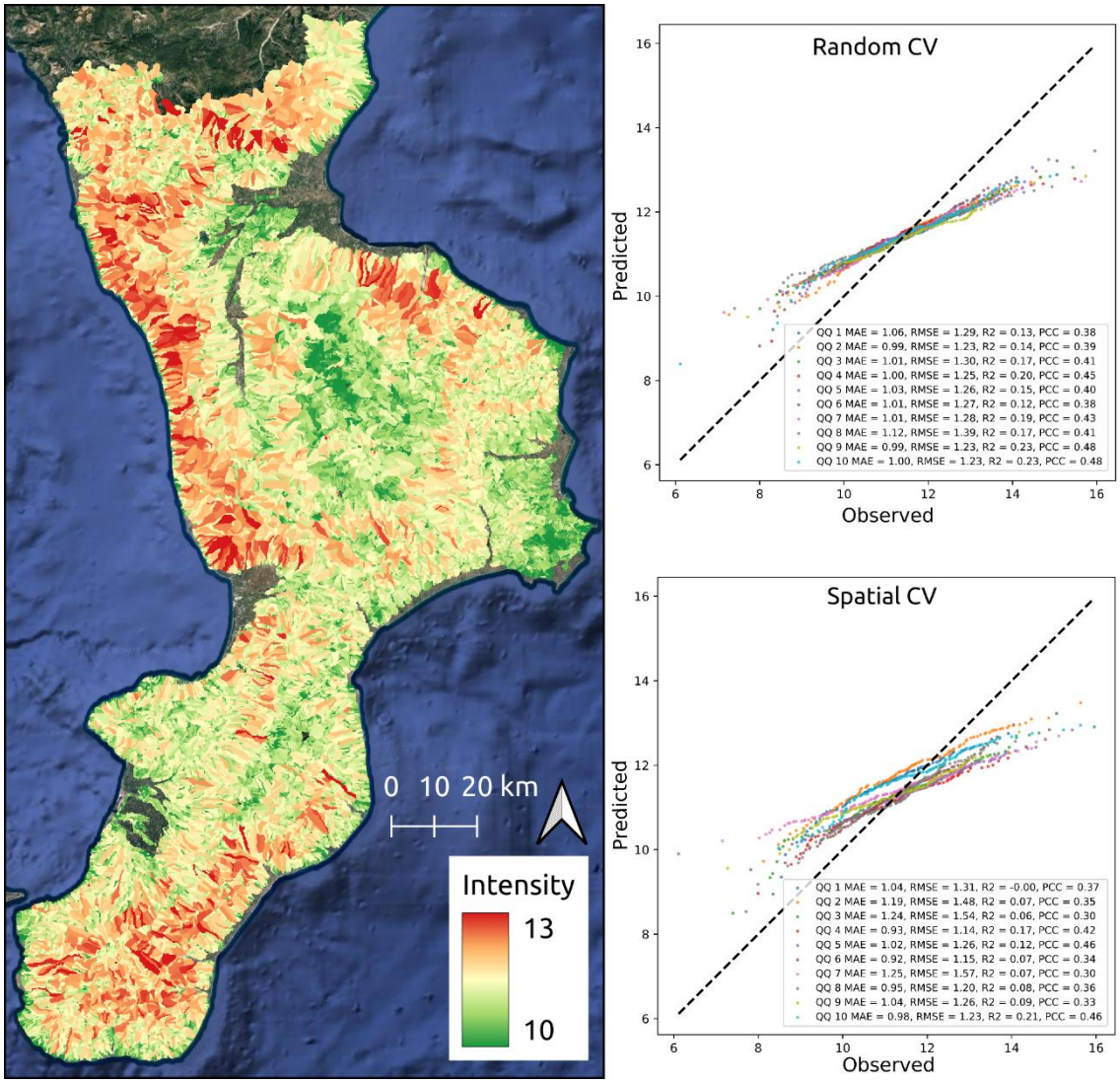

Figure 24. Landslide intensity map and the relative random and spatial cross-validation metrics.

4. References

Akgun, V., Erkut, E., & Batta, R. (2000). On finding dissimilar paths. European Journal of Operational Research, 121(2), 232–246. https://doi.org/10.1016/S0377-2217(99)00214-3.

Alvioli, M., Guzzetti, F., & Marchesini, I. (2020). Parameter-free delineation of slope units and terrain subdivision of Italy. Geomorphology, 358, 107124. https://doi.org/10.1016/j.geomorph.2020.107124.

ANSFISA – Agenzia Nazionale per la Sicurezza delle Ferrovie e delle Infrastrutture Stradali e Autostradali. (2022). Istruzioni operative per l'applicazione delle Linee guida per la classificazione e gestione del rischio, la valutazione della sicurezza ed il monitoraggio dei ponti esistenti.

Atkinson, Alexander L., et al. (2017). Assessment of runup predictions by empirical models on non-truncated beaches on the south-east Australian coast. Coastal Engineering, 119, 15-31. https://doi.org/10.1016/j.coastaleng.2016.10.001.

Basalamah, S. (2020). A Visual Analytics System for Route Planning and Emergency Crowd Evacuation. International Journal of Advanced Computer Science and Applications (IJACSA)11.2. http://dx.doi.org/10.14569/IJACSA.2020.0110284.

Blais-Stevens A., & Behnia, P. (2016). Debris flow susceptibility mapping using a qualitative heuristic method and Flow-R along the Yukon Alaska Highway Corridor, Canada. Natural Hazards and Earth System Sciences, 16(2), 449–462. https://doi.org/10.5194/nhess-16-449-2016.

Breiman, L. (1996). Bagging predictors. Machine Learning, 24(2), 123–140. https://doi.org/10.1007/BF00058655.

Breiman, L. (2001). Random Forests. Machine Learning, 45(1), 5–32. https://doi.org/10.1023/A:1010933404324.

Bruno, G., Pignone, F., Silvestro, F., Gabellani, S., Schiavi, F., Rebora, N., Giordano, P., & Falzacappa, M. (2021). Performing hydrological monitoring at a national scale by exploiting rain-gauge and radar networks: the Italian case. Atmosphere, 12(6), 771. https://doi.org/10.3390/atmos12060771.

Carrara, A., Cardinali, M., Guzzetti, F., & Reichenbach, P. (1995). GIS technology in mapping landslide hazard. Geographical Information Systems in Assessing Natural Hazards; Springer: Dordrecht, The Netherland: 135-175.

Cavalli, M., & Grisotto, S. (2006). Individuazione con metodi GIS delle aste torrentizie soggette a colate detritiche: applicazione al bacino dell'alto Avisio (Trento), vol. 26, Nuova Bios, Idronomia Montana, pp. 1–11.

Chow, V.T. (1962). Hydrologic determination of waterway areas for the design of drainage structures in small drainage basins. University of Illinois Engineering Experiment Station Bulletin No. 462, Urbana, IL, 104 p. https://core.ac.uk/download/pdf/4814575.pdf [Last access: 15 October 2025]

Cianflone, G., Larosa, S., Beccaro, L., Viscomi, A., Tolomei, C., Chiodo, G., ... & Dominici, R. (2025). A revised landslide inventory of the Calabria Region (Italy). Journal of Maps, 21(1), 2421292. https://doi.org/10.1080/17445647.2024.2421292.

Claps, P., Ganora, D., Apostolo, A., Brignolo, I., and Monforte, I. (2020a). Catalogo delle Piene dei Corsi d'acqua Italiani Vol. 1, Ed. CINID., 499 pp., ISBN 978-88-945568-0-3.

Claps, P., Ganora, D., Apostolo, A., Brignolo, I., and Monforte, I. (2020b). Catalogo delle Piene dei Corsi d'acqua Italiani Vol. 2, Ed. CINID, 537 pp., ISBN 978-88-945568-2-7.

Claps, P., Ganora, D., Apostolo, A., Brignolo, I., and Monforte, I. (2020c). Catalogo delle Piene dei Corsi d'acqua Italiani Vol. 3, Ed. CINID, 401 pp., ISBN 978-88-945568-4-1.

Claps, P., Evangelista, G., Ganora, D., Mazzoglio, P., & Monforte, I. (2023). FOCA (Italian FlOod and Catchment Atlas). Zenodo [data set]. https://doi.org/10.5281/zenodo.10446258.

Claps, P., Evangelista, G., Ganora, D., Mazzoglio, P., & Monforte, I. (2024). FOCA: a new quality-controlled database of floods and catchment descriptors in Italy. Earth System Science Data, 16, 1503–1522. https://doi.org/10.5194/essd-16-1503-2024.

Choe, T., Kim, J., Shin, M., Kim, K., & Kim, M. (2023). Complex disaster response framework to reduce urban disaster vulnerability. Science Progress, 106(1), 368504231152770. https://doi.org/10.1177/00368504231152770.

Dahal, A., & Lombardo, L. (2023). Explainable artificial intelligence in geoscience: a glimpse into the future of landslide susceptibility modeling. Computers & Geosciences, 176, 105364. https://doi.org/10.1016/j.cageo.2023.105364.

European Commission - Joint Research Centre (2016). Global flood depth-damage functions: Methodology and the database with guidelines. Publications Office. https://data.europa.eu/doi/10.2760/16510.

Fannin, R.J., & Wise, M.P. (2001). An empirical-statistical model for debris flow travel distance. Canadian Geotechnical Journal, 38(5), 982–994. https://doi.org/10.1139/t01-030.

Fusco, F., Abbate, A., Calcaterra, D., De Vita, P., Guerriero, L., Longoni, L., & Papini, M. (2023). Susceptibility mapping of shallow landslides inducing debris flows: a comparison of physics-based approaches. Italian Journal of Engineering Geology and Environment, 1, 63-71. https://doi.org/10.4408/IJEGE.2023-01.S-09.

Gariano, S. L., Petrucci, O., & Guzzetti, F. (2015). Changes in the occurrence of rainfall-induced landslides in Calabria, southern Italy, in the 20th century. Natural Hazards and Earth System Science, 15(10), 2313-2330. https://doi.org/10.5194/nhess-15-2313-2015.

Grelle, G., Soriano, M., Revellino, P., Guerriero, L., Anderson, M.G., Diambra, A., Fiorillo, F., Esposito, L., Diodato, N., & Guadagno, F.M. (2014). Space-time prediction of rainfall-induced shallow landslides through a combined probabilistic/deterministic approach, optimized for initial water table conditions. Bulletin of Engineering Geology and the Environment, 73, 877-890. https://doi.org/10.1007/s10064-013-0546-8.

Hack, J. (1957). Studies of longitudinal stream profiles in Virginia and Maryland. US Geological Survey Professional Paper, 294-B, United States Government Printing Office, Washington (USA), 1.

Holman, R.A. (1986). Extreme value statistics for wave run-up on a natural beach. Coastal Engineering, 9(6), 527-544. https://doi.org/10.1016/0378-3839(86)90002-5.

Jowett, I.G. (1998). Hydraulic geometry of New Zealand rivers and its use as a preliminary method of habitat assessment. Regulated Rivers: Research & Management, 14, 451–466. https://doi.org/10.1002/(SICI)1099-1646(1998090)14:5%3C451::AID-RRR512%3E3.0.CO;2-1.

Kirpich, Z. (1940). Time of concentration of small agricultural watersheds. Civ. Eng. 10(6), 362.

Leopold, L.B., & Maddock, T. (1953). The Hydraulic Geometry of Stream Channels and Some Physiographic Implications. Geological Survey Professional Paper 252. https://pubs.usgs.gov/pp/0252/report.pdf [Last access: 15 October 2025].

Linsley, R.K., Jr., Kohler, M.A., & Paulhus, J.L.H. (1958). Hydrology for Engineers, McGraw-Hill, 340 pp.

Loche, M., Alvioli, M., Marchesini, I., Bakka, H., & Lombardo, L. (2022). Landslide susceptibility maps of Italy: Lesson learnt from dealing with multiple landslide types and the uneven spatial distribution of the national inventory. Earth-Science Reviews, 232, 104125. https://doi.org/10.1016/j.earscirev.2022.104125.

Lombardo, L., Tanyas, H., Huser, R., Guzzetti, F., & Castro-Camilo, D. (2021). Landslide size matters: a new data-driven, spatial prototype. Engineering Geology, 293, 106288. https://doi.org/10.1016/j.enggeo.2021.106288.

Manfreda, S., & Samela, C. (2019). A digital elevation model based method for a rapid estimation of flood inundation depth. Journal of Flood Risk Management, 12(S1), e12541. https://doi.org/10.1111/jfr3.12541.

Mase, H. (1989). Random wave runup height on gentle slope. Journal of Waterway, Port, Coastal, and Ocean Engineering, 115(5), 649-661. https://doi.org/10.1061/(ASCE)0733-950X(1989)115:5(649).

Ministero delle Infrastrutture e della Mobilità Sostenibili (2022). Linee guida per la classificazione e gestione del rischio, la valutazione della sicurezza ed il monitoraggio delle gallerie esistenti. Consiglio Superiore dei Lavori Pubblici, Parere n. 29/2022, 8 April 2022.

McEnroe, B.M., & Zhao, H. (1999). Lag times and peak coefficients for rural watersheds in Kansas. University of Kansas, USA, Report No. K-TRAN: KU-98-1. https://rosap.ntl.bts.gov/view/dot/14157 [Last access: 15 October 2025].

Navarro, J. S., Zhuang, R., Albertini, C., & Manfreda, S. (2025). Mapping flood susceptibility using Random Forest exploiting satellite observations and geomorphic features. Science of The Total Environment, 1002, 180592. https://doi.org/10.1016/j.scitotenv.2025.180592.

NERC (1975). Hydrological studies, in Flood studies report, London, England.

Nielsen, P. (2009). Coastal and estuarine processes. Vol. 29. World Scientific Publishing Company.

Nobre, A.D., Cuartas, L.A., Momo, M.R., Severo, D.L., Pinheiro, A., & Nobre, C.A. (2016). HAND contour: A new proxy predictor of inundation extent. Hydrological Processes, 30(2), 320–333. https://doi.org/10.1002/hyp.10581.

Poate, T.G., McCall, R.T., & Masselink, G. (2016). A new parameterisation for runup on gravel beaches. Coastal Engineering, 117, 176-190. https://doi.org/10.1016/j.coastaleng.2016.08.003.

Reichenbach, P., Rossi, M., Malamud, B.D., Mihir, M., & Guzzetti F. (2018). A review of statistically–based landslide susceptibility models. Earth-Science Reviews, 180, 60-91. https://doi.org/10.1016/j.earscirev.2018.03.001.

Ruggiero, P., Komar, P.D., McDougal, W.G., Marra, J.J., & Beach, R.A. (2001). Wave runup, extreme water levels and the erosion of properties backing beaches. Journal of Coastal Research, 407-419.

Samela, C., Troy, T.J., & Manfreda, S. (2017). Geomorphic classifiers for flood-prone areas delineation for data-scarce environments. Advances in Water Resources, 102, 13–28. https://doi.org/10.1016/j.advwatres.2017.01.007.

Samela, C., Carisi, F., Domeneghetti, A., Petruccelli, N., Castellarin, A., Iacobini, F., Rinaldi, A., Zammuto, A., & Brath, A. (2023). A methodological framework for flood hazard assessment for land transport infrastructures. International Journal of Disaster Risk Reduction, 85, 103491. https://doi.org/10.1016/j.ijdrr.2022.103491.

Schulz, E.F. (1969). Dimensionless unit hydrographs from tropical watersheds. Presented at the National Fall Meeting American Geophysical Union, December 15-18, San Francisco, California, USA. https://mountainscholar.org/handle/10217/648 [Last access: 15 October 2025].

SCS (1972). National Engineering Handbook, Section 4, Hydrology. Washington, D.C., U.S. Dept. of Agriculture. First published as: Hydrology guide for use in watershed planning. http://irrigationtoolbox.com/NEH/Part%20630%20Hydrology/neh630-ch15.pdf [Accessed 19 July 2023]

Stockdon, H.F., et al. (2006). Empirical parameterization of setup, swash, and runup. Coastal Engineering, 53(7), 573-588. https://doi.org/10.1016/j.coastaleng.2005.12.005.

Titti, G., Hu, L., Festi, P., Elia, L., Borgatti, L., & Lombardo, L. (2025). An updated version of the SZ-plugin: from space to space-time data-driven modeling in QGIS. International Journal of Applied Earth Observation and Geoinformation, 142, 104679. https://doi.org/10.1016/j.jag.2025.104679.

Trigila, A., Iadanza, C., & Spizzichino, D. (2010). Quality assessment of the Italian Landslide Inventory using GIS processing. Landslides, 7(4), 455-470. https://doi.org/10.1007/s10346-010-0213-0.

Vousdoukas, M.I., Wziatek, D., & Almeida, L.P. (2012). Coastal vulnerability assessment based on video wave run-up observations at a mesotidal, steep-sloped beach. Ocean Dynamics, 62(1), 123-137. https://doi.org/10.1007/s10236-011-0480-x.

Watt, W.E., & Chow, K.C.A. (1985). A general expression for basin lag lime. Can. J. Civ. Eng. 12, 294-300.

Williams, J.R. (1968). Runoff hydrographs from small Texas Blacklands watersheds. ARS 41-143. USDA-ARS.